University of Nevada, Reno

COMPLIANT, LARGE-STRAIN, AND SELF-SENSING TWISTED STRING ACTUATORS WITH APPLICATIONS TO SOFT ROBOTS

A Thesis Submitted in Partial Fulfillment

of the Requirements for the Degree of Master of Science in

Mechanical Engineering

by

David Bombara

Dr. Jun Zhang / Thesis Advisor

August 2022

THE GRADUATE SCHOOL

We recommend that the thesis
prepared under our supervision by

entitled

be accepted in partial fulfillment of the
requirements for the degree of

Advisor

Committee Member

Graduate School Representative

Markus Kemmelmeier, Ph.D., Dean
Graduate School

ABSTRACT

The twisted string actuator (TSA) is a rotary-to-linear transmission system that has been implemented in robots for high force output and efficiency. The basic components of a TSA are a motor, strings, and a load (to keep the strings in tension). The twisting of the strings shortens their length to generate linear contraction. Due to their high force output, energy efficiency, and compact form factor, TSAs hold the potential to improve the performance of soft robots. Currently, it is challenging to realize high-performance soft robots because many existing soft or compliant actuators exhibit limitations such as fabrication complexity, high power consumption, slow actuation, or low force generation. The applications of TSAs in soft robots have hitherto been limited, mainly for two reasons. Firstly, the conventional strings of TSAs are stiff and strong, but not compliant. Secondly, precise control of TSAs predominantly relies on external position or force sensors. For these reasons, TSA-driven robots are often rigid or bulky.

To make TSAs more suitable for actuating soft robots, compliant, large-strain, and self-sensing TSAs are developed and applied to various soft robots in this work. The design was realized by replacing conventional inelastic strings with compliant, thermally-activated, and conductive supercoiled polymer (SCP) strings. Self-sensing was realized by correlating the electrical resistance of the strings with their length. Large strains are realized by heating the strings in addition to twisting them. The quasi-static actuation and self-sensing properties are accurately captured by Preisach hysteresis operators. Next, a data-driven mathematical model was proposed and experimentally validated to capture the transient decay, creep, and hysteretic effects in the electrical resistance. This model was then used to predict the length of the TSA, given its resistance.

Furthermore, three TSA-driven soft robots were designed and fabricated: a three-

fingered gripper, a soft manipulator, and an anthropomorphic gripper. For the three-fingered gripper, its fingers were compliant and designed to exploit the Fin Ray Effect for improved grasping. The soft manipulator was driven by three TSAs that allowed it to bend with arbitrary magnitude and direction. A physics-based modeling strategy was developed to predict this multi-degree-of-freedom motion. The proposed modeling approaches were experimentally verified to be effective. For example, the proposed model predicted bending angle and bending velocity with mean errors of 1.58° (2.63%) and 0.405 °/sec (4.31%), respectively. The anthropomorphic gripper contained 11 TSAs; two TSAs were embedded in each of the four fingers and three TSAs were embedded in the thumb. Furthermore, the anthropomorphic gripper achieved tunable stiffness and a wide range of grasps.

I dedicate this thesis to my family, who always encouraged me to dream big.

ACKNOWLEDGEMENTS

I firstly thank my thesis advisor, Dr. Jun Zhang. I cannot thank him enough for the invaluable mentorship and guidance. Beginning when I was undergraduate, Dr. Zhang introduced me to this research field and worked closely with me to train me for academia. As one of the first students to join his lab, he worked closely with me to develop me into a competent researcher. He provided me recommendation letters that helped me land several highly-competitive internships, scholarships, fellowships, and offers to Ph.D. programs. I am thankful for having received the 2020–2021 Graduate Dean's Merit Scholarship from the University of Nevada, Reno (UNR), the 2021–2022 NASA Space Technology Graduate Research Opportunities (NSGTRO) fellowship, and the National Science Foundation Graduate Research Fellowship (starting in the autumn of 2022). I am truly fortunate to have worked for Dr. Zhang.

Secondly, I thank the fellow students from the research group (the Smart Robotics Lab). Ph.D. students Revanth Konda and Thulani Tsabedze were amazing mentors and friends. Revanth worked closely with me on multiple research projects, providing a valuable set of skills that complemented my own. Steven Swanbeck, an undergraduate researcher, was extremely helpful as we worked together in the final year of my master's degree. I thank Ryan Coulter, a current Ph.D. student at UNR, for his assistance with projects during the spring of 2021. I also thank Ember Chow, a recent graduate with a Bachelor of Science in the Department of Intelligent Systems Engineering at Indiana University Bloomington, for her assistance with projects during the summer of 2021. I also thank Aaron Wiese, Steven Fowzer, Sean Ross, Lyndie Munson, Vasiliy Mansurov, and Edwin Abrego, who were undergraduate engineering researchers that I worked closely with during my time as an undergraduate researcher in the Smart Robotics Lab from the fall of 2018 to the spring of 2020.

Thirdly, I thank the thesis committee members, Dr. Matteo Aureli and Dr. Hao

Xu, for dedicating their valuable time to serve on the committee. I thank them for providing excellent instruction on control theory during the multiple courses of theirs that I took. Both professors provided recommendation letters that helped me get selected for scholarships, nationally-competitive fellowships, and top-ranked Ph.D. programs.

Fourthly, I thank the researchers and engineers that worked with me during my remote internship for NASA Langley Research Center, during the first year of my master's degree studies: Dr. Hyun Jung Kim, Dr. Calum Williams, and Mr. Stephen Borg. Although my research for that internship was not included in this thesis, these researchers provided valuable mentorship and guidance that helped me grow as a researcher. With their help, I published a first-authored journal paper on my NASA internship research. I also gained skills that I applied to my master's degree research. Each of them also provided me with glowing recommendation letters for nationally-competitive fellowships and top-ranked Ph.D. programs.

Fifthly, I thank Evan Laske at NASA Johnson Space Center, who has been a remarkable research collaborator during my time as a fellow for the NSTGRO program. Mr. Laske has provided a valuable perspective on robotic gripping for outerspace applications. This work was supported in part by a NASA Space Technology Graduate Research Opportunities award (Grant #80NSSC21K1282).

Last but not least, I thank my family. My parents do not have bachelor degrees, but they highly valued education. They always encouraged my siblings and I to excel in our studies, whether we were in kindergarten or graduate school. I will be the first of my four siblings to obtain a graduate degree, let alone one in engineering. My parents especially sacrificed a lot so that my siblings and I could attend undergraduate and graduate school. This thesis is proof that their efforts have been worthwhile.

TABLE OF CONTENTS

LIST OF TABLES

LIST OF FIGURES

CHAPTER 1

INTRODUCTION

1.1 Conventional Robots and Actuators

Since their inception, robots have been conventionally powered by rigid electrical or fluidic actuators [2]. This actuation strategy enables high force output and speed. In addition, the rigidity and predictability of these actuators enable accurate modeling from the first principles. However, a consequence is that robots have so far been mostly confined to structured environments in repetitive or strictly-defined tasks. For example, robotic manipulators have generally been confined to factory production lines. In addition, the traditional actuation methods and rigid robots can be inherently bulky, heavy, or costly. Rigid actuators and robots require highly accurate control, lest they damage their environment if a robotic manipulator deviates from its reference trajectory, for example. These limitations motivate the development of soft (compliant) actuators and robots that will enable robots to operate in new environments and accelerate their mass use by society.

1.2 Artificial Muscle Actuators

Artificial muscle actuators have recently spurred great interest for their capability to overcome the limitations of conventional actuators. The motivation for artificial muscle research is in the quest for a new "gold standard" in actuation. For traditional robots, the electromagnetic motor is the current gold standard. The ideal artificial muscles will perform on par or better than natural skeletal muscle in all aspects.

There are currently some artificial muscles that outperform skeletal muscle in at least one aspect, but no artificial muscle outperforms in all aspects [3]. Artificial muscles produce mechanical work that is driven by a variety of stimuli, such as heat, voltage, pressure, magnetic fields, and even light [3, 4]. (Note that despite their name, artificial muscles do not yet mimic the biochemistry of natural muscle [2].) Advances in artificial muscles over the past 30 years have been driven by advances in nanomaterial fabrication and other advanced fabrication processes [5]. Artificial muscles tend to possess traits that approach those of natural skeletal muscle: high power densities, high force output densities, and inherent compliance [3]. These actuators have shown strong potential in a wide range of robots, such as manipulators, grippers, prosthetics, exo-skeletons, medical robots, and soft robots [3].

Artificial muscles show great promise. However, they tend to exhibit limitations at their current stage of technological development. These include (1) fabrication complexity [6, 7], (2) high power requirement [8, 9], (3) slow actuation [10, 11], and (4) insufficient force generation [12, 11, 13]. Dielectric elastomer actuators (DEAs) and hydraulically amplified self-healing electrostatic (HASEL) actuators generate sufficient actuation, but it is challenging to realize their complicated and high-cost fabrication procedures [7, 9]. DEAs and HASEL actuators also demand high-voltage generators that are not only costly but also potentially dangerous. Magnetorheological (MR) elastomers generate acceptable ranges of force and displacement, but they require large rigid parts to generate magnetic fields which are utilized for actuation [14, 15]. This could lead to difficulty in including them in compact devices. Similarly, pneumatic actuators exhibit appreciable strain and force generation, but adopting them in robotic devices demands the inclusion of pumps or compressors [16, 17]. Furthermore, the thermal actuation of shape-memory alloys (SMAs) [10, 18, 19] not only results in low bandwidth and low force generation, but also could be dangerous and cause damage to the robots in which they are employed. In addition, ionic polymer-metal composite (IPMC) actuators generate decent strains at low voltages, but exhibit low power-density and low stress output [3, 13].

1.3 Soft Robotics

1.3.1 Overview of Soft Robots

Soft robots are often, but not necessarily, driven by soft (artificial muscle) actuators. As the name implies, a soft robot is one whose body is primarily composed of materials with low elastic moduli [20]. Since robots may be constructed from materials with wide ranges of elastic moduli, the soft–rigid distinction of a robot is more like a continuum than a dichotomy. Numerous useful motions have been achieved using soft robots. These include grasping, crawling, walking, and swimming [21, 22, 23, 6, 24, 25, 26, 27].

1.3.2 Limitations of Soft Robots

Soft robots hold much potential to overcome the limitations of conventionally rigid robots. However, soft robots still suffer from limitations, as they are still in their technological infancy (relative to rigid robots). The main limitations of soft robots are that (1) they tend operate with low forces and speeds and (2) they are challenging to model and control.

Low actuation force and speed is a common problem in soft robots. High-speed soft robots generally output low forces, and vice versa [3]. A completely soft robot will conform to a surface upon contact. This will cause its force to be distributed over a larger surface area, and thus exert lower pressures on that surface. This behavior can be mitigated by rigid endo/exoskeletons or tunable stiffness mechanisms.

The low stiffness of soft robots makes them inherently difficult to model and control. The robots' soft bodies undergo large macroscopic strains during actuation [2]. This movement paradigm fundamentally differs from rigid robots, which move via components that rotate or slide against each other (i.e. via prismatic or revolute joints) [28]. Soft robots consequently often possess infinite degrees of freedom (DOF) [28]. However, this also means that soft robots are typically underactuated, in which case it is impossible to actively control every DOF [28]. Although many strategies for soft robotic modeling have been proposed, it remains an open research problem [28].

The difficulty in modeling soft robots leads to difficulty in controlling soft robots. Another challenge is in maintaining a particular robot configuration under the influence of gravity [28]. For example, a soft robotic finger will droop due to its own weight [29]. The many degrees of freedom that soft robots have also make trajectory planning difficult [30]. Recent work developed a simulator to evaluate reinforcement learning (RL)-based control policies for soft robots [30]. However, model-based methods may be preferred to RL-based methods, so long as the model does not exhibit prohibitively high computational complexity.

1.4 The Twisted String Actuator (TSA)

1.4.1 Overview of the TSA

In-between the purely rigid actuators and the purely soft artificial muscles exist the twisted string actuator (TSA). Some consider the TSA to be an artificial muscle [3], whereas other classify it as a transmission system [31]. The TSA consists of an electric motor that twists multiple attached strings (Fig. 1.1(a)). The twisting of the strings shortens their length to generate linear actuation [3]. The key advantage of the TSA is its ability to act as a high-reduction rotary-to-linear gear, without requiring a rigid and complicated gear train [32]. This rotary-to-linear conversion is over 85% energy-efficient [3]. In addition, the direction of linear actuation is inline and parallel to the motor's rotational axis. This property contrasts the motor and spool, in which the motor is perpendicular to the linear actuation. The TSA also leaves great flexibility in its design: robots on nearly any macroscopic scale can be created, based on the size of the motor and strings. TSAs already have been applied to experimental robots, such as robotic gloves [33], haptic devices [34], rigid grippers [35], and exoskeletons [36].

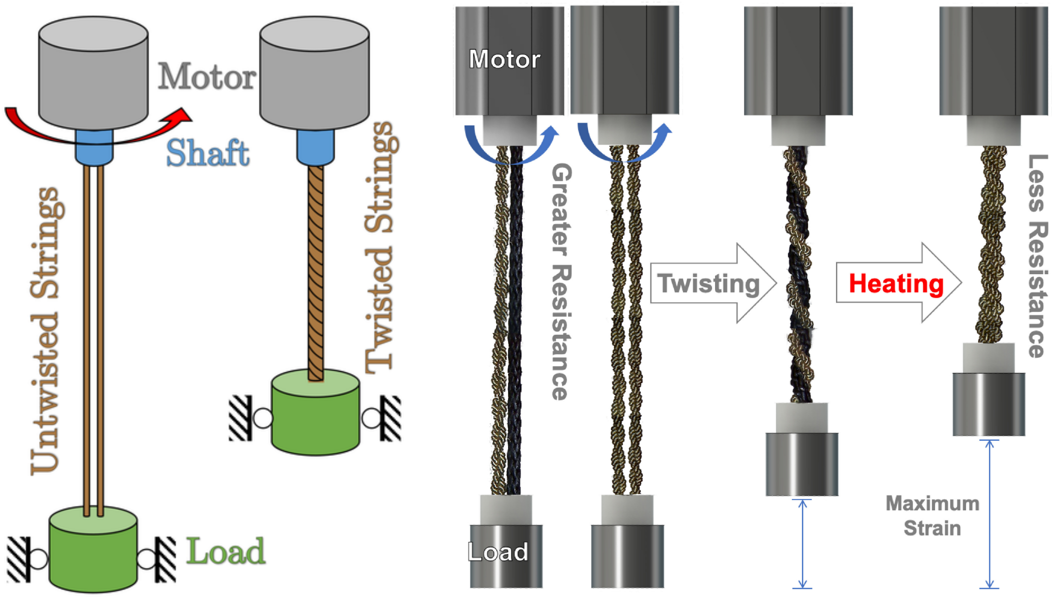

(a) (b)

Figure 1.1: (a) Diagram of a conventional twisted string actuator (TSA). (b) Illustration of the proposed novel TSA, with one or two supercoiled polymer (SCP) strings instead of typical strings made with ultra-high-molecular-weight polyethylene (UHMWPE). As the strings twist, the load moves linearly and the strings' electrical resistance decreases. Additional strain can be obtained in the TSA with SCP strings via Joule heating.

Mathematical models are well-developed for the TSA whose strings are in-extensible. Using the geometry of the strings, dynamical models of twists versus length and angular speed versus linear contraction speed have been developed and verified for TSAs [31]. In addition, the required motor torque to compensate for the tension in the strings at every motor angle within the working range has been modeled [37]. The dynamical model of torque versus twists that accounts for string friction and compliance showed significant improvement over the static model [37].

1.4.2 Limitations of the TSA

Despite the advantages of TSAs, they have generally been difficult to use in soft robotic applications for the three main reasons discussed below.

Firstly, the existing TSAs predominantly rely on strings with high stiffness but low compliance (with some exceptions [38]). Compliance is a key performance metric of soft actuators. It is crucial that actuators are compliant, such that the generated robot motions are effective and safe to the soft robot body and the surrounding environment [39]. Compliance is one of the most important advantages of systems like collaborative robots, medical robots, and robotic exo-suits [40, 41, 42, 43]. Compliance can be difficult to achieve when the actuator must operate with high force outputs or speeds. Previous studies used strings such as braided ultra-high-molecular-weight polyethylene (UHMWPE) strings, commonly referred to as Dyneema string [32]. The stiffness of these strings, normalized to their unit length, is often over 3000 N. Highly stiff strings allow for simpler modeling by considering the strings as inextensible. Those strings can lift high loads and reliably perform for thousands of cycles or more [44, 45]. TSAs with compliant strings have been realized before. For example, a robotic joint utilized compliant and elastic strings [38]. In soft robots, compliant actuators are more desirable. However, recent studies showed that the maximum strain of TSAs decreased when their compliance was increased [46]. This may because the twisting causes increased longitudinal tension force on the strings that stretches them. There is a need to simultaneously increase the compliance and the strain of the TSA.

Secondly, closed-loop control of TSAs predominantly requires external rigid sensors. This is undesirable for soft robotic applications due to the increased stiffness, mass, and volume. Important advantages of soft robots over their rigid counterparts are compliance, compactness, and low mass. Therefore, maintaining system compliance and reducing the need for external sensors are desired. Previous studies developed models that related the number of motor rotations to the linear contraction of the TSA. However, the utilization of those developed models often required externally-attached motor encoders or other external sensors for closed-loop control [31, 47, 48, 44]. In addition to being rigid, external sensors increase system mass, volume, and complexity. Self-sensing TSAs could overcome this issue. In self-sensing, an electrical signal that is inherent to the actuator is used to predict a mechanical signal (linear contraction). The electrical signal may then be straightforwardly digitized by a microcontroller/computer to control the TSA's length.

Thirdly, there is a lack of work integrating TSAs into soft robots. This is likely because motors are required to construct TSAs and are thus difficult to be incorporated into soft structures. Meanwhile, the successful applications of TSAs in exoskeletons and assistive devices [49, 33, 50] demonstrate their strong promise in areas where safe interaction with humans is necessary. Although the strings used in traditional TSAs are not stretchable, the compliant properties of the twisting configuration could be very useful in soft robots. Furthermore, by employing stretchable strings, the compliance of the TSAs could be greatly enhanced.

1.5 Supercoiled Polymer (SCP) Strings

1.5.1 Thermal Actuation

The supercoiled polymer (SCP) string was originally invented in 2014 as a thermally-driven linear artificial muscle actuator [51]. This fiber-based actuator may be fabricated from a variety of materials, including conductive nylon polymers, carbon nanotube yarns, fishing lines, or sewing filaments [3]. As thermal actuators, SCPs have shown promising performance metrics: linear contractions of 10–20% and power densities up to 27 W/g [3]. They have been used in applications such as robotic gloves [52] and hands [11].

This study takes advantage of SCP strings' thermal actuation. SCP actuators integrated into other compliant and soft actuators have enabled improved functionality and performance. For example, SCP strings combined into a soft pneumatic actuator allowed for a soft robot with variable stiffness [53]. In another study, combining an SCP actuator with a shape memory alloy (SMA) actuator led to a large-stroke and powerful soft actuator [54].

1.5.2 Self-Sensing

While most of the existing studies employed SCP strings as actuators [55, 56], there is a recent interest in adopting SCP strings as sensors. In [57], a linear relationship between the resistance and the length of SCP strings was observed, and it was proposed that SCP strings could be used as position sensors with application to soft robots. Abbas and Zhao demonstrated that both the applied load and change in length of conductive coiled thread can be used to determine resistance change in SCPs [58]. SCP strings manufactured from graphite power and nylon threads were also used as position sensors in [59]. It is thus promising to incorporate the SCP strings into TSAs for strain sensing.

1.6 Contribution

Twisted string actuators, with high force output and fast motors, could potentially be used in soft robots to offset some of these robots' disadvantages. The main contributions of this thesis as follows:

1. Fabrication and experimental characterization of compliant, large-strain, and self-sensing TSAs by using SCPs (Fig. 1.1(b)). These TSAs were realized by replacing the typical inextensible strings in TSAs with stretchable SCP strings. Experimental characterization was conducted under a variety of actuator configurations and conditions.
2. Modeling of the actuation and self-sensing properties of these compliant and large-strain TSAs.
   - Both twisting-induced actuation and thermally-induced actuation (linear contraction) were modeled under quasi-static inputs. The Preisach model is adopted to capture the evident hysteresis in the input–output correlations.
   - The self-sensing property (resistance-length correlation) is firstly modeled under quasi-static inputs, then transient inputs. The electrical resistance exhibited transient decay, hysteresis, and creep. The transient decay is modeled using a polynomial of logarithms. The hysteresis is modeled using a Prandtl-Ishlinskii model. The creep is modeled using a second-order discrete time state-space model.
3. Development of soft robots actuated by twisted strings. These included a three-fingered gripper, a soft-body manipulator, and an anthropomorphic gripper.

- Three-fingered gripper: SCP-based TSAs were integrated into the gripper that enable self-sensing and combined thermally-induced and twisting-induced actuation. The gripper also utilized the Fin Ray Effect for improved grip [60].
- Soft manipulator: A physics-based model was proposed that predicted the position of the manipulator in 3D space. The model synthesized the existing modeling strategies of TSAs and soft robots to facilitate continuous control of the manipulator's end-point position in 3D space.
- Anthropomorphic gripper: A tunable stiffness mechanism was designed into the anthropomorphic gripper to enable the gripping of a wider range of objects. A monolithic multi-DOF soft robotic thumb was developed that was driven by TSAs. This enabled the gripper to efficiently realize different grasp types.

The SCP-based self-sensing TSAs were fabricated in two versions (schemes). *Scheme 1* consisted of a single SCP paired with a single non-conductive and inextensible string. *Scheme 2* consisted of two SCP strings. With *Scheme 2*, larger strains were realized by combining thermally-induced actuation of the SCPs with twisting-induced actuation of the TSAs. Extensive experimental characterizations of the quasi-steady-state, transient, and lifetime self-sensing properties were conducted. Next, mathematical equations were derived from the experimental data to predict the relationship between electrical resistance and length. The model was verified on a separate experimental data set and showed high accuracy.

The TSA-driven soft robots showcased the utility of TSAs in soft robotic devices. For the three-fingered gripper, design, fabrication, and grasping demonstrations were completed. The gripper used antagonistic TSAs, which have been modeled in previous work [61]. For the TSA-driven soft robotic manipulator, the design, fabrication, experimental characterization, and physics-based modeling were completed. For the anthropomorphic soft gripper, design, fabrication, and grasping demonstrations were presented. Because the design of each finger in the anthropomorphic gripper was similar to the design of the soft robotic manipulator, the anthropomorphic soft gripper may be modeled using the same strategy as the soft manipulator.

1.7 Document Organization

The thesis is organized as follows. Chapter 2 details the fabrication and experimental characterization of compliant, large-strain, and self-sensing TSAs. Chapter 3 details the modeling of these TSAs. Chapter 4 details the development of the three different TSA-driven soft robots: the three-fingered gripper, the soft manipulator, and the anthropomorphic gripper. Finally, the conclusion and remarks on future work are presented in Chapter 5.

CHAPTER 2

DESIGN AND CHARACTERIZATION OF COMPLIANT, LARGE-STRAIN, AND SELF-SENSING TWISTED STRING ACTUATORS

This chapter details the design and characterization of compliant, large-strain, and self-sensing TSAs [46, 62, 63, 64]. Experimental characterization was completed under both quasi-static inputs [63] and transient inputs [64].

2.1 Design and Fabrication

Below, decisions on the materials, string thicknesses, fabrication processes, and experimental procedures for the proposed TSA are discussed.

Firstly, the compliance of the SCP strings meant increased loads elongated the TSA. Stiffness measurements were taken to quantify the compliance of the resulting TSAs. Because the TSAs may have different lengths, the stiffness normalized to the length was reported, consistent with existing studies [48, 31]. Instead of N/m, the normalized stiffness had units of N.

Secondly, TSAs consisting of two strings of equal length were adopted in this study. TSAs can be fabricated from different numbers of strings [65], but using two strings is most common. For combined twisting-induced and thermally-induced actuation, the TSA was fabricated from one or two conductive SCP strings. It was observed that TSAs made from one UHMWPE string and one SCP string underwent negligible length change under applied voltage. For self-sensing, two string configurations were studied during twisting-induced actuation. In the first configuration (*Scheme 1*), the TSA was fabricated from one regular UHMWPE string and one conductive SCP string (Fig. 2.1(a)). The SCP string underwent detectable resistance change as the TSA contracted. The inextensible string made from braided UHMWPE allowed the TSA to support heavier loads. In *Scheme 2*, the TSA was fabricated from two SCP strings (Fig. 2.1(b)).

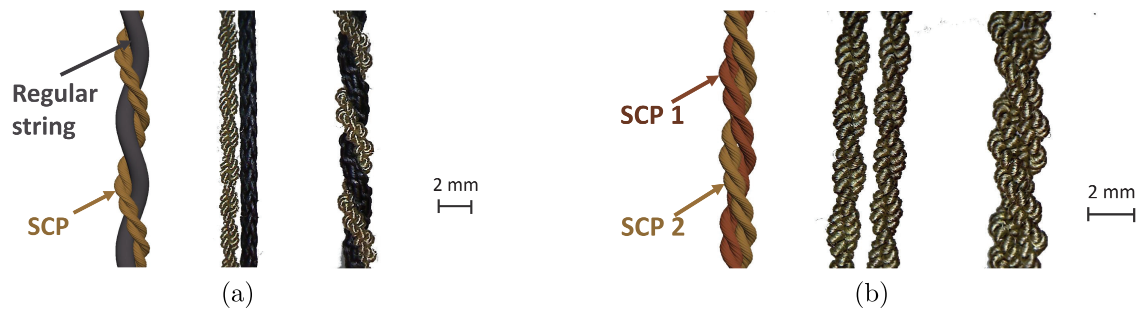

Figure 2.1: (a) *Scheme 1*: A TSA consisting of a super-coiled polymer (SCP) string and a regular string. (b) *Scheme 2*: A TSA consisting of two SCP strings.

Thirdly, for actuation and self-sensing, TSAs with different diameters were studied. The diameter of the TSA which was determined by the ply number of the SCP string. The ply number was the number of silver-coated nylon threads used to fabricate each string. This study utilized silver-coated nylon 66 threads (110/34 dtex Z turns High Conductive Yarn, V Technical Textiles). When the TSA was utilized for combined twisting-induced and thermally-induced actuation, relatively thin strings were utilized. Thin strings allowed for quicker Joule heating and therefore quicker actuation. 3-ply and 4-ply strings were tested with diameters of 0.72 mm and 0.89 mm, respectively. The diameter of the resulting TSA depended on the amount of actuation — its diameter increased as the TSA linearly contracted via motor rotations or Joule heating. When the TSA was utilized purely for self-sensing, both thin and thick strings were studied. In this study, 4-ply strings were considered thin and 8-ply strings were considered thick. Thick strings were tested for self-sensing because of their ability to support heavier loads, making them suitable for practical robotic applications that require high strength.

Finally, the TSA linearly contracted due to motor rotations, but only up to a limited amount. The maximum contraction was reached at the maximum input voltage and maximum motor rotations. The maximum voltage was the greatest voltage at which the SCP string did not overheat and break. The maximum number of motor rotations was the point when additional rotations did not cause additional actuation, but instead buckled and eventually snapped the strings.

The fabrication of the proposed TSA consisted of four steps. The schematic of the procedure is shown in Fig. 2.2.

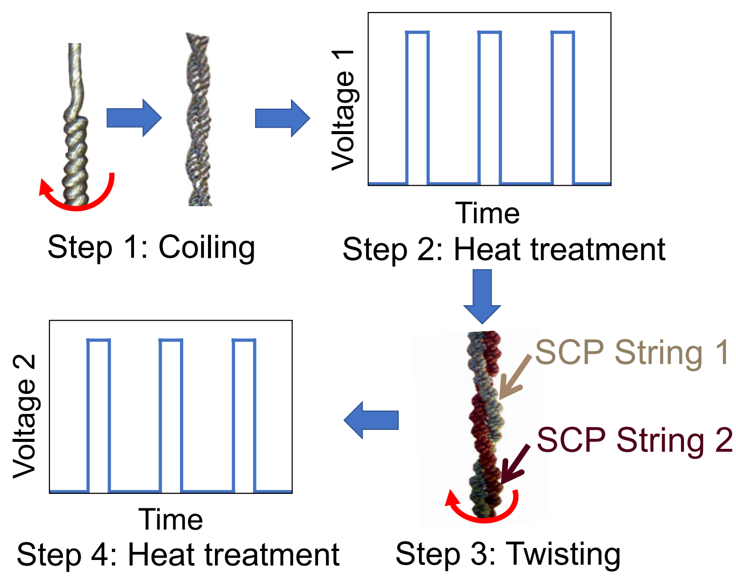

Figure 2.2: The fabrication process of the proposed TSA is composed of four steps: coiling, heat treatment, twisting, and a second heat treatment.

Step 1: Coil Conductive Nylon Threads: Firstly, a given number of conductive nylon threads were attached to a motor shaft and hung vertically. A load suspended from the threads kept them under tension while ensuring they remained fixed at the bottom. Previous studies found that SCPs achieved poor performance under low amounts of tension or no tension at all [21, 51]. The motor rotated clockwise until the threads formed spring-like coils. The coiled structure was then stabilized by double-backing the threads, which balanced the torque induced from twist insertion. This process followed previous approaches [55, 56]. If SCP strings were not thermally actuated and only used for self-sensing in TSAs, the fabrication of the SCP string was finished in this step. In that case, the SCP strings from this step were combined to form a TSA, as long as the strings had equal length and diameter. If the strings were actuated thermally, additional steps were required.

Step 2: Heat Treat SCP Strings: Next, the SCP strings from Step 1 were annealed via Joule heating, in which voltage pulses were applied to the strings while the strings suspended a load [51, 11]. Oven-based heat treatment could have been used instead [51]. Approximately 10 cycles of heat treatment were necessary, with voltage on for 7–10 s and off for 90 s. The peak voltage was 24 V. The peak current depended on the electrical resistance of the SCP string. 3-ply and 4-ply SCP strings had peak currents of 0.53 A and 0.70 A, respectively. The hanging load during heat treatment also depended on the diameter of the SCP string. For 3-ply and 4-ply SCP strings, 150 g, and 200 g were used, respectively. An SCP string was sufficiently heat treated when its resting length no longer increased between cycles. At this point, the SCP string generated approximately 15% strain consistently. Attempts to heat treat past 15% strain led to increased probability of breakage. The maximum attainable strain depended on various factors, such as the string material, thickness, voltage pulse width, and pulse amplitude. Because SCP-based TSAs have not yet been realized by other research groups, there is no direct comparison to other research groups' studies. However, the maximum thermally-induced strain of an SCP-based TSA was similar to the maximum thermally-induced strain of an individual SCP. Repeatable strains of individual non-mandrel-coiled SCP strings in the literature (not twisted in the TSA configuration) have varied between approximately 10% [11] and 20% [51].

Step 3: Fully Twist Two SCP Strings: After heat treating individual SCP strings in Step 2, two SCP strings were combined to form a TSA. In the TSA, the top ends of the string were fixed to a motor's shaft. At the bottom ends of the strings, a linear movement toward or away from the motor was permitted but rotation was restricted. To keep the compliant strings taut, a load was suspended from the bottom of them. During preliminary experiments, the SCP-based TSAs loaded with no mass exhibited negligible thermal-based actuation. The magnitude of the load was the same amount used during experiments. The motor then rotated until the TSA achieved its maximum possible strain. Because the motor rotated clockwise in Step 1, the motor also rotated clockwise in this step. When the two SCP strings were fully twisted about each other, contact between them was maximized and another heat treatment process was conducted.

Step 4: Heat Treat Twisted SCP-Based TSAs: Lastly, the fully-twisted SCP-based TSA was heat treated. In addition to heat treatment in Step 2, the SCP strings in this configuration were found to require additional heat treatment. This was likely because the strings were now in a new configuration. Instead of hanging individually, the two SCP strings hung together, twisted in tight physical and electrical contact. As in Step 2, voltage pulses heated the strings in cycles. Heat treatment in this step was complete when the TSA demonstrated a consistent 15% thermally-activated strain. The number of cycles and peak voltage needed to obtain this strain varied. For two 3-ply SCP strings, five cycles were sufficient. Each cycle consisted of voltage on for 10 s and off for 100 s. The peak voltage was 10 V and the peak current was 0.86 A. The peak voltage in this step was lower than in Step

2. In this step, the overall structure was thicker and shorter because the SCP strings were fully twisted together. Consequently, the electrical resistance between each end of this structure was lower than in Step 2. Lower electrical resistance meant greater electrical power when the same voltage was applied. To compensate and prevent the actuators from burning, the peak voltage was lowered.

2.2 Experimental Setup

The TSA was mounted vertically with a stepper motor (NEMA 17HS4401 with A4988 driver) at the top, SCP strings in the middle, and the load at the bottom, as shown in Fig. 2.3. A custom-designed printed circuit board (PCB) measured the electrical resistance. The PCB was mounted near the motor and featured a hole that allowed the SCP strings to maintain electrical contact with copper leads during rotation. The stepper motor and SCP strings were electrically decoupled to prevent the energizing motor coils from inducing noise in the resistance measurement during actuation. The SCP strings were heated by manually connecting positive and negative alligator clips.

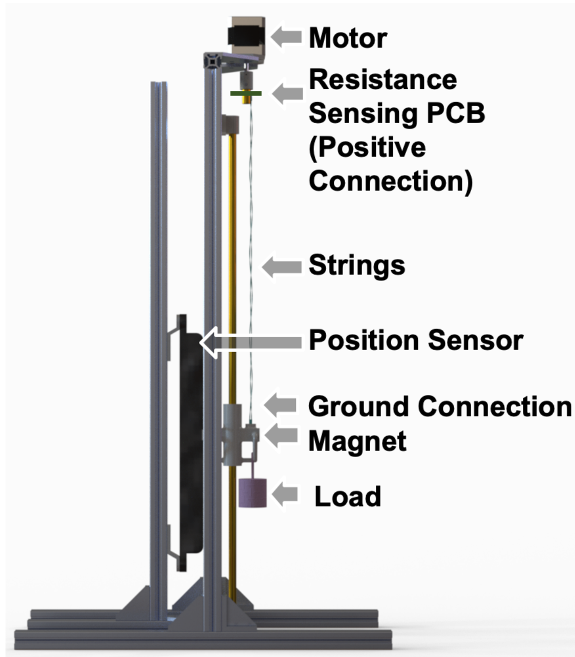

Figure 2.3: The experimental setup utilized to twist the SCP strings and measure the resistance for strain self-sensing of the compliant TSA.

Experiments were automated with a microcontroller based on the ATmega2560 microchip. A 16-bit ADC (ADS1115, Adafruit) connected to the microcontroller discretized the length measurement captured by an analog magnetoresistive position sensor (SPS-L225-HALS, Honeywell). The position sensor had a resolution of 0.14 mm and a sensing range of 225 mm. The resistance of the TSA was calculated by applying a precise current (50 mA $\pm$ 5 μA) from a current source (AD8276, Analog Devices), then measuring the voltage across the strings. A 20-bit ADC (CS5513, Cirrus Logic) enabled 0.240 $\mu\Omega$ resistance measurement resolution.

2.3 Compliance

The stiffness of the proposed TSAs was quantified by the equation below. Stiffness is inversely proportional to length, so in this study, the normalized stiffness with respect to length was reported. Previous work on TSAs reported the normalized stiffness [61, 37].

$$K = F \cdot \frac{L_0}{L - L_0}, \tag{2.1}$$

where K is the normalized stiffness with respect to length, F is the applied load, L_0 is the length of the actuator with no load, and L is the length of the actuator under the loading force of F.

Firstly, the compliance of the SCP strings was quantified by their normalized stiffness. To obtain this metric, loads were suspended from the strings in increasing and decreasing sequences. Each load remained on the string for 60 s, to ensure the length reached its steady state. The length of the SCP string was then recorded, similar to our previous work [66]. The results in Fig. 2.4(a)–(b) exhibit mild hysteresis, which is consistent with previous studies [66, 56].

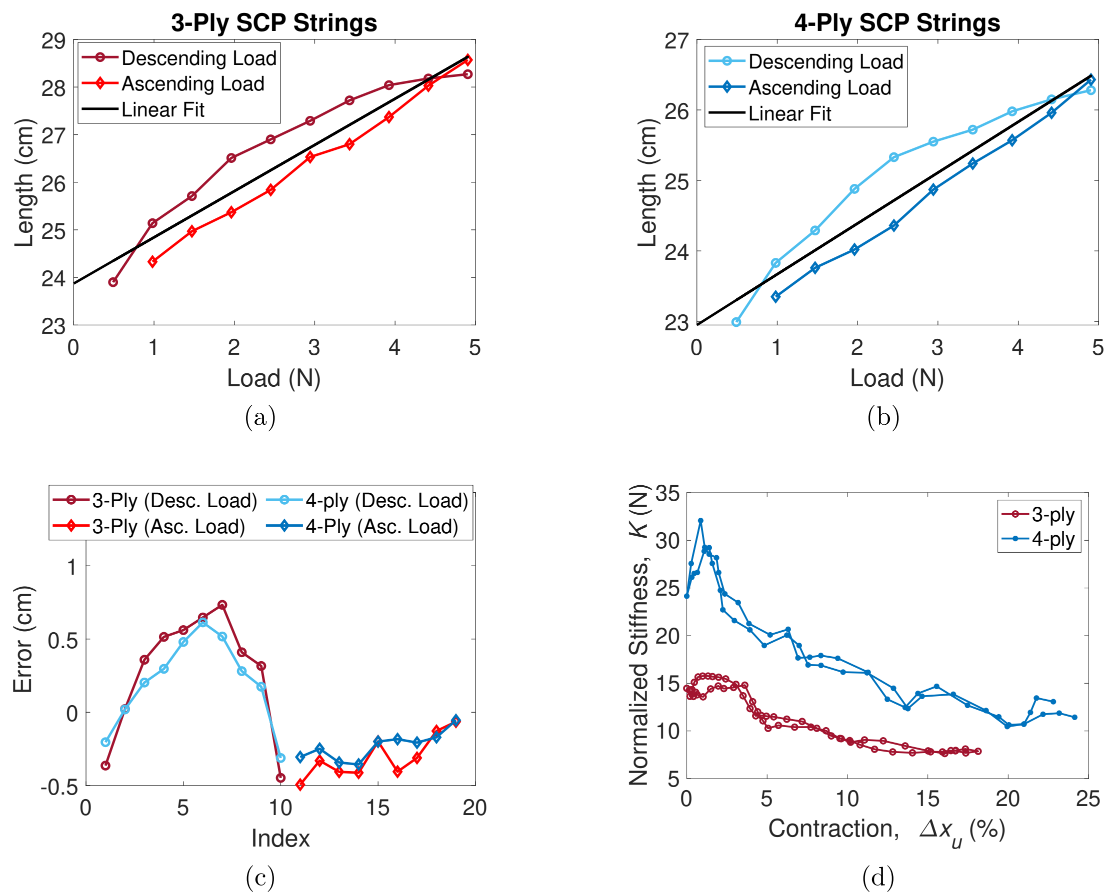

Figure 2.4: Results for the stiffness characterization. (a) The measurements of length and load of single 3-ply and (b) 4-ply SCP actuators used to calculate their stiffness. (c) The error of the linear model of the stiffness of the SCP strings calculated at each data point. (d) The calculated normalized stiffness of the 3-ply and 4-ply TSAs as a function of contraction percentage.

The stiffness of the SCP string was found by approximating the length–load relationship with a linear fit. Fig. 2.4(c) shows the strain modeling error as a percentage of the experimentally-obtained strain. The average absolute modelings errors were computed to be 0.37±0.57 cm and 0.27±0.42 cm for 3-ply and 4-ply strings, respectively. The maximum and minimum modeling errors were 0.733 cm and -0.494 cm, respectively. Based on the linear model, the 3-ply and 4-ply strings were computed to have normalized stiffnesses of 24.61 N and 31.88 N, respectively. "Index" in Fig.

2.4(c) is the numbering of experimentally-obtained length values. Because it was normalized to the length unit, the normalized stiffness had units of N instead of N/m. SCP strings were shown to be significantly more compliant than conventional TSA strings [32]. Previous work considered the viscoelastic properties of SCP strings [67]. However, applying viscoelastic theory to model the compliance of the individual SCPs and SCP-based TSAs was beyond the scope of this study.

The normalized stiffnesses of 3-ply and 4-ply TSAs are given in Fig. 2.4(d) as a function of contraction percentage. Although the stiffness was mildly hysteretic (Fig. 2.4(d)), the stiffness of each TSA generally decreased as contraction increased. This relationship was consistent with stiff strings in existing studies [31]. Mild fluctuations in stiffness due to noise and the system setup were observed, but this was consistent with previous work [45]. A previous study by Palli et al. on the modeling and control of TSAs obtained the normalized stiffness as a function of motor rotations [31]. Palli et al. found that the stiffness of 20 N-loaded and 30 N-loaded TSAs peaked at approximately 16 motor rotations, then generally decreased as motor rotations increased. In this study, the stiffness was calculated by measuring the changes in length due to changes in loading. The stiffnesses of the TSAs were generally lower than the stiffnesses of corresponding 3-ply and 4-ply strings. TSAs made from 4-ply strings notably had greater stiffness because they were thicker. Utilizing relatively small changes in loading decreased the fluctuations observed in Fig. 2.4(d).

2.4 Actuation

2.4.1 Performance Metrics

For TSAs actuated by heat and motor rotations in this section, the contraction of the TSA, Δx_u, was evaluated according to the equation below:

$$\Delta x_u = \frac{x_l - x}{x} \times 100\%, \tag{2.2}$$

where x_l is the length of the loaded TSA with no twists or voltage inputs. x is the length of the TSA after twisting and/or voltage inputs.

2.4.2 Twisting-Induced Actuation

In this case, SCP strings were passively used in TSAs and no heat was applied. The length of the TSA was measured at each corresponding motor rotation. The input motor rotations changed as a function of time. Fig. 2.5(a) shows both the input motor rotations and corresponding contraction of a 4-ply TSA loaded with 250 g. The data indicated that mild disturbances may have been caused by unaccounted friction in the setup. However, accounting for noise and disturbance was beyond the scope of the study.

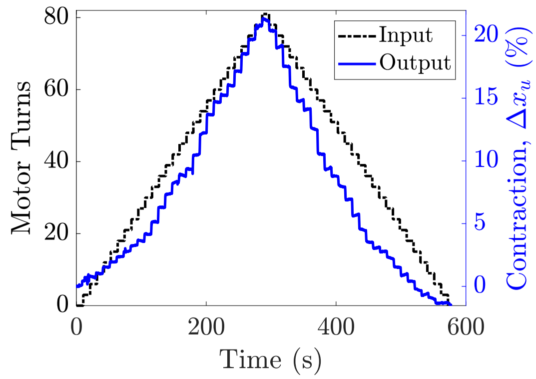

(a)

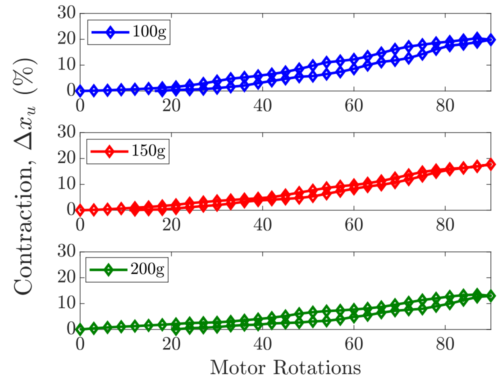

(b)

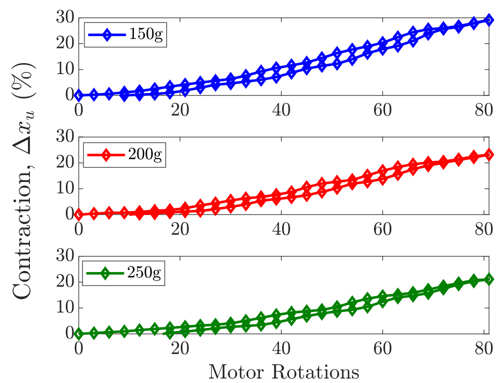

(c)

Figure 2.5: (a) The input motor rotations and resulting TSA contraction versus time. The relationship between length and motor rotations for (b) 3-ply strings and (c) 4-ply strings under different loading conditions.

TSAs made from thin 3-ply SCP strings were tested with three different loads: 100 g, 150 g, and 200 g. TSAs made from 4-ply strings are able to withstand slightly higher loads. Therefore, they were tested with 150 g, 200 g, and 250 g. The results for 3-ply and 4-ply strings are shown in Fig. 2.5(b) and 2.5(c), respectively. Hysteresis between motor rotations and linear contraction existed in all experiments. This was likely due to the physical properties of the silver-coated nylon strings [66]. In addition, friction likely existed between the two strings, as well as between plies within each string as the TSA twisted.

2.4.3 Combined Twisting-Induced and Thermally-Induced Actuation

In this case, both motor rotations and Joule heating were applied to the TSAs to obtain a larger amount of strain. The SCP strings were considered active because of their ability to contract under applied heat, which was also utilized to further actuate the proposed TSA.

The experiment to obtain the maximum strain was conducted as follows. After fully twisting the strings, voltage inputs were monotonically applied in steps from zero to maximum, then back to zero, and the strings finally fully untwisted. The maximum voltage varied according to the thickness and tension of the actuator. Too much voltage burned and broke the actuator, whereas too little voltage yielded little movement. The maximum voltage was chosen as follows: first a number of extreme tests were conducted, then the maximum voltage was chosen to be slightly less than the extreme experiments. The voltage input sequence and resulting TSA contraction are plotted in Fig. 2.6(a) with respect to time. Note that the voltage sequence was slow; it was expected that the steady-state temperature was obtained. For example, the pair of 4-ply SCP strings loaded with 250 g achieved a maximum contraction of 14.1% via thermal actuation after initially twisting 81 full rotations. The contraction mildly fluctuated, which may have been due to small environmental disturbances or friction in the setup. Accounting for this was beyond the scope of the work. More work will be done in the future to make the TSA's length measurements smoother and more consistent.

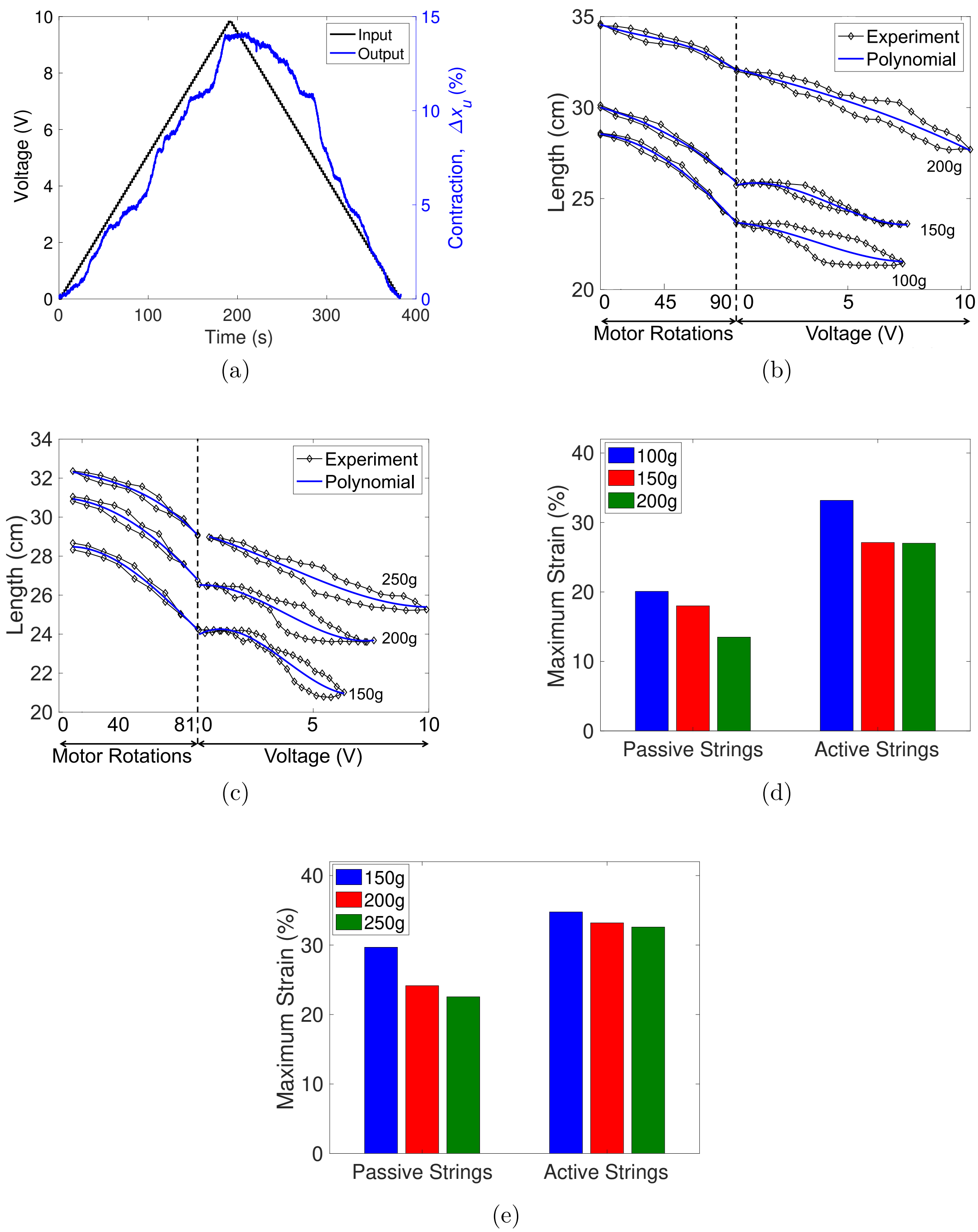

Figure 2.6: (a) The input voltage to the TSA and resulting contraction versus time. Experimental results and polynomial models for length–voltage and length–twisting correlations for TSAs made with (b) 3-ply strings and (c) 4-ply strings under different loading conditions. A summary of results, detailing the maximum strains obtained for passive and active (d) 3-ply SCP strings and (e) 4-ply SCP strings.

Fig. 2.6(b) and 2.6(c) show the complete actuation of TSAs made from 3-ply and 4-ply strings, respectively. To compare the performance of each TSA fairly, each TSA was tested with the same loading and input motor rotations as when SCP strings were only used passively. As an example, for the TSA with 3-ply strings under 200 g load, the TSA achieved 13.49% strain with passive strings and 27.01% strain with active strings, showing a 13.51% increase in maximum strain with thermally-induced actuation.

The comparison of maximum strain between active and passive strings is summarized in Fig. 2.6(d) (3-ply strings) and Fig. 2.6(e) (4-ply strings). TSAs made from 3-ply and 4-ply SCP strings averaged 29.10% and 33.51% maximum strain, respectively. These averages were 11.91% and 8.05% larger, respectively, than when TSAs were only twisted. When the strings were only twisted, 3-ply and 4-ply TSAs respectively achieved 17.19% and 25.46% maximum strain. As shown in Fig. 2.6(d)–(e), when only twisting was used, the maximum strain of the TSAs depended significantly on their loading. However, when both heating and twisting actuated the TSA, the maximum strain changed less significantly with the amount of loading (except for the 100g-loaded 3-ply TSA with active strings).

The temperature of the SCP-based TSA determined its length. The time for the proposed TSA to heat was relatively quick, but the time for it to cool was longer. Under a step voltage input, the SCP fully actuated within a few seconds, but the time for complete cooling was over one minute. This was because of the noticeable creep behavior due to inherent nylon material properties [68]. This amount of time also increased as the thickness of the SCP strings increased. Modeling of this time-dependent behavior was beyond the scope of this work.

2.5 Self-Sensing

2.5.1 Quasi-Static Characterization

In this section, a series of experiments were conducted to obtain the correlation between the resistance and length of TSAs. Two self-sensing schemes were tested. *Scheme 1* used one TSA with one UHWMPE string and one SCP string. *Scheme 2* used one TSA with two SCP strings. Two types of SCP strings were tested with different thicknesses. A “thin” SCP string was made with four nylon threads whereas a “thick” SCP string was made with eight nylon threads. Different loading conditions were also tested to evaluate the length–resistance correlations.

To measure and capture the relationship between the resistance and length of TSAs, the following procedures were employed. Firstly, the TSA was manufactured either with one SCP string and one regular string, or with two SCP strings. A weight was used to generate a constant loading condition for the TSA. Secondly, the motor generated a sequence of rotations to change the length of TSA. Each rotation was held for 3 minutes, ensuring that the steady-state length and resistance was reached. The correlation between the steady-state length and resistance was obtained based on the measurements.

Experiments were firstly conducted to measure the relationship between the length and resistance of the TSA composed of one thin SCP string and one UHMWPE string (*Scheme 1*). Sequences of rotations ranging from $[20, 55]$ were used, as shown in Fig. 2.7(a). The steady-state length and resistance values were measured. As shown in Fig. 2.7(b), by twisting the TSA, its length decreased from 28 cm to 21 cm. This generated over 25% contraction. Two loading conditions were tested, one with 450 g of weight, and the other was 550 g. The corresponding length–resistance correlation measurements were provided in Fig. 2.7(c). As shown, there was an evident correlation between resistance and length — the resistance increased with increasing length. This can be explained as follows. When the motor generated fewer rotations, the TSA became longer. The distances between the adjacent coils of the SCP string were also larger, thus producing a larger resistance value. Under a larger loading condition, the TSA became longer and produced a larger resistance. The results were consistent with existing studies of using SCP strings as sensors [69].

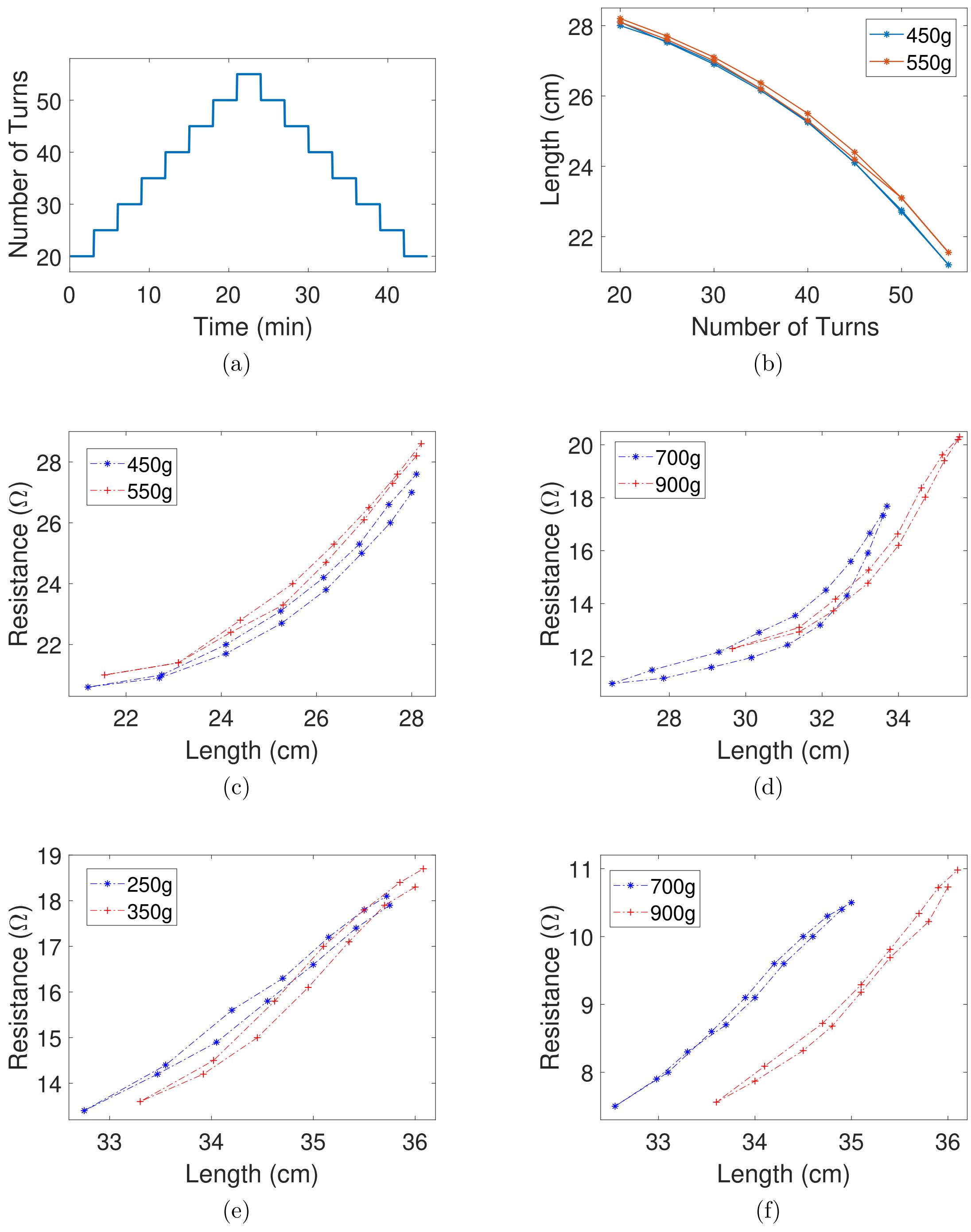

Figure 2.7: Experimental results for characterization of the quasi-static relationship between electrical resistance and length. (a) The motor rotation sequence versus time. (b) The length of the TSA with different numbers of motor rotations. (c)–(d) Results for *Scheme 1*, where the TSA has one SCP string and one UHMWPE string. (c) Results for *Scheme 1* using a thin SCP and (d) thick SCP string. (e)–(f) Results for *Scheme 2*, where each TSA has two SCP strings. Results using (e) thin strings and (f) thick strings.

Tests were also conducted for thicker TSAs whose SCP string was fabricated with 8-ply nylon threads. Similarly, rotation sequences generated different TSA contractions. Fig. 2.7(d) shows the correlation between the length and resistance of the TSA under 700 g and 900 g loading conditions.

Next, experiments were conducted for TSAs that possessed two SCP strings (*Scheme 2)*. For the 4-ply SCPs under one twisting-untwisting cycle and two different loading conditions (250 g and 350 g), the resistance and length data were recorded and shown in Fig. 2.7(e). Furthermore, thicker (8-ply) SCP strings were also used for TSAs. Fig. 2.7(f) shows its length–resistance relationship under 700 g and 900 g loading conditions.

Experiments demonstrated clear relationships between the length and resistance of the SCP-based TSAs, albeit with mild hysteresis. The relationship between the TSA's length and SCP string's resistance was less hysteretic for the configuration of *Scheme 2* (two SCP strings twisting around each other), as shown in Fig. 2.7(c)–(f). For *Scheme 1* (TSA with one SCP and one UHMWPE string), the sensing range was much larger than *Scheme 2*. In *Scheme 1*, over 6 cm of length change was demonstrated, while for *Scheme 2*, the actuation range of the TSA was 2–3 cm, as shown in Fig. 2.7(c)–(f). Compared to *Scheme 2*, *Scheme 1* withstood larger weight due to higher tensile strength of the polyethylene string.

The resistance of the TSA increased with a larger length. Therefore, greater loading conditions generally increased the resistance in SCP strings. The changes in resistance in *Scheme 1* and *Scheme 2* were due to the increased tension exerted on the SCPs during twisting. The other cause for this phenomenon, specifically in *Scheme 2*, was the increase in the contact between the SCP strings during twisting. This led to an increase in conductivity and consequently decrease in resistance.

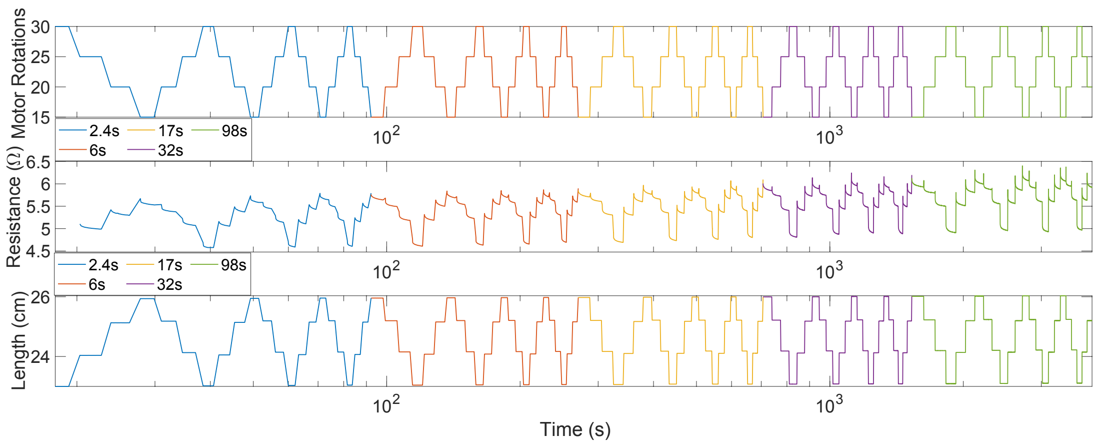

(a)

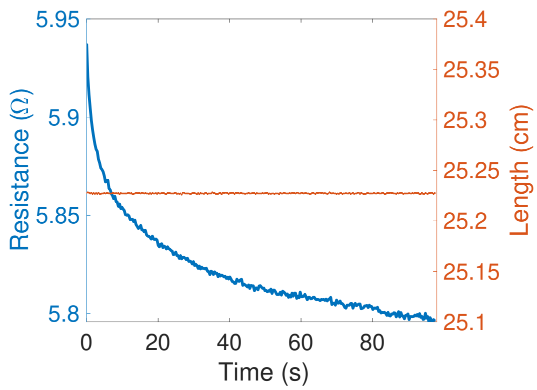

(b)

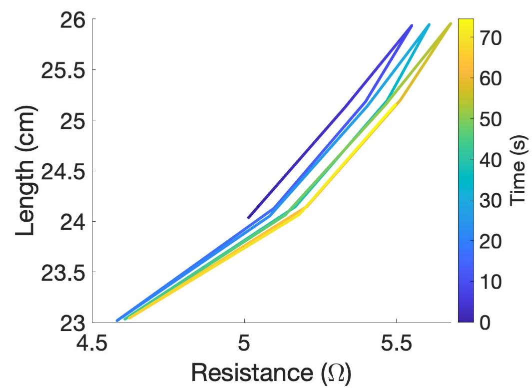

(c)

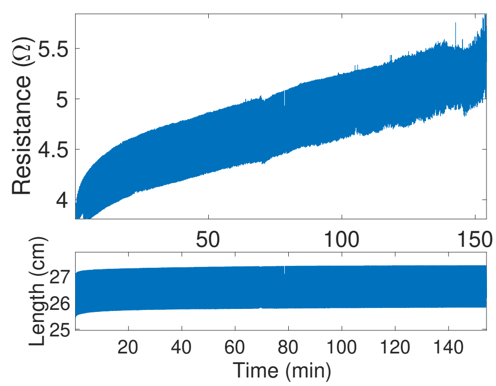

(d)

Figure 2.8: Transient experimental characterization. (a) The motor rotation input sequence and experimental measurements of resistance and length for five sets of experiments with different twisting and step durations. (b) The transient resistance and length measurements versus time while the motor was at rest. (c) The relationship between resistance and length for the case of 2.4 s step duration displayed hysteresis and creep. (d) The resistance and length were plotted for 596 complete rotation cycles, lasting over two hours.

2.5.2 Transient Characterization

Fig. 2.8(a) shows the experimental measurements of the transient actuator length and resistance on a logarithmic time scale for a TSA with a 350 g load. During one cycle, the resistance of the TSA was greater at greater lengths and fewer string twists. As the strings twisted more, the TSA decreased in length and increased in diameter. Consequently, the SCP strings were in greater electrical contact, which reduced the resistance. After the motor rotated, spikes in resistance were noticed in the first data point after the motor rotated, as shown in Fig. 2.8(a). In addition, the strain-resistance measurements exhibited three behaviors, namely, transient decay, hysteresis, and creep.

Transient Decay

Experiments showed that the resistance transiently decayed after any amount of string twists and step durations, as shown in Fig. 2.8(a)–(b). As time increased, the rate of resistance decay decreased until reaching a steady state after approximately two minutes. In addition, the length of the TSA remained constant during this time, as shown in Fig. 2.8(b). The transient resistance decay suggested that there was inductance in the SCP strings' conductive coils. After each rotation, TSA underwent a spike in applied current from 0 mA to 50 mA. This current was necessary to measure the resistance of the twisted SCP strings. In general, the inductance of a coil varies with the square of the number of turns in the coil [70]. In future work, the stretched exponential function[71] could be utilized to describe the transient resistance decay.

Hysteresis

Under symmetric motor rotation input (Fig. 2.8(a)), the length output was not symmetric (Fig. 2.8(c)). The quasi-static relationship between resistance and length showed hysteresis, as shown in Fig. 2.8(c). Previous studies found hysteresis individually in both TSAs and SCP actuators [55, 66]. Hysteresis has previously been revealed in a variety of smart materials, elastic materials, and ferromagnetic materials [72, 73].

Creep and Self-Sensing Lifetime

The creep of the resistance measurement was evident as the number of cycles increased, as shown in Fig. 2.8(d). The length of the TSA demonstrated mild creep within the first ten minutes of the test and then became negligible. The lifetime of the self-sensing property in TSAs was experimentally tested for 596 cycles lasting over two and a half hours. To do so, the TSA was loaded with a 550-g load and twisted in the following manner. After initially twisting the strings 15 twists, the motor rotated for two turns at a time, then paused for one second, repeatedly until the string reached 25 twists. This input sequence was repeated for the entire duration of the test. The creep in resistance over many cycles for other materials was observed in previous work [74]. The cause of creep was perhaps due to friction between the two SCP strings during twisting. As the strings twisted, the silver coating may have gradually worn off over time to make the strings less conductive. A previous study on the lifetime of TSAs found that friction and heat contributed to the deformation and degradation of the strings [45]. However, those experiments were conducted at 2000 rpm, nearly 10 times the speed of the TSA used in this work. In addition, the TSA was tested at loads of 3–20 kg [45], which was much greater than the loads used in this study. Due to these reasons, evident temperature increases were not observed. However, the temperature of the strings may likely have increased slightly during the experiments. Measuring the TSA's temperature is beyond the scope of this study.

CHAPTER 3

PARAMETER FITTING OF COMPLIANT, LARGE-STRAIN, AND SELF-SENSING TWISTED STRING ACTUATORS

This chapter details the modeling of the large-strain actuation and self-sensing in the compliant TSA [46, 62, 63, 64]. The combined twisting-induced and thermally-induced actuation is modeled under quasi-static inputs and outputs [63]. The self-sensing TSA (its resistance–strain correlation) is modeled under both quasi-static and transient inputs [63, 64].

Note that the modeling in this study is not physics–based. Parameters are fitted to previously-developed models for hysteresis and creep [75, 76]. Although physics-based modeling is not employed in this work, the "black box" modeling strategy has precedent in previous studies on smart materials and artificial muscles [76, 55].

3.1 Modeling of TSA Strain

A Preisach operator was used to capture the actuation and self-sensing properties of TSAs. A linear model was also considered for comparison purposes.

3.1.1 Hysteresis Model

Although there are many ways to model hysteretic materials and structures, the Preisach model is one of the most effective and widely used. This model is composed of a weighted superposition or integral of a continuum of delayed relays [72, 73]. The weight distribution is discretized to facilitate the real-time implementation and computation of the Preisach operator [73]. The model's computational complexity increases as the discretization level, M, increases. A discretization level between 10 and 40 is most commonly chosen [72].

The hysteresis model of the twisting-induced and thermally-induced actuation is the sum of two distinct Preisach models. The discretized Preisach model for twisting-induced actuation is:

$$L_{\text{Preisach}}(T) = \sum_{i=1}^{M} \sum_{j=1}^{M+1-i} \lambda_{ij} w_{ij}(T) + b_T, \tag{3.1}$$

where T is the input twists and b_T is a constant offset. λ_{ij} is the discretized weight identified from experiments and $w_{ij}(T)$ is fully dependent on the input twist history.

Similarly, voltage-induced actuation can be described as:

$$L_{\text{Preisach}}(V) = \sum_{i=1}^{M} \sum_{j=1}^{M+1-i} \mu_{ij} y_{ij}(V) + b_V, \tag{3.2}$$

where V is the constant input voltage and b_V is the constant offset. The discretized weight μ_{ij} is often different than λ_{ij} in Eq. (3.1). $y_{ij}(V)$ fully depends on the input voltage history. The discretization level M remains the same as in Eq. (3.1). The constant voltage was considered to be a surrogate of temperature, and the correlation between constant voltage and length of SCP strings has been considered in our recent studies [55, 77]. Other artificial muscles also require the use of a temperature surrogate when a direct temperature measurement is not available. For example, a 2016 study used electrical current as a temperature surrogate in the self-sensing of vanadium oxide microactuators [78]. A first-order thermoelectric model can also relate the electrical power across an SCP to its temperature [11].

To find the overall length of the TSA, the outputs from twisting-induced and voltage-induced actuation are summed. The formula is additive because the actuation was sequential (first through twisting, then through voltage).

$$L = L_{\text{Preisach}}(T) + L_{\text{Preisach}}(V), \tag{3.3}$$

where L is the overall length of the TSA. In reality, the effects of voltage and twists on the length of the TSA may be coupled. However, during this study, the TSA is heated only after being fully twisted. In other words, this model does not apply when heat and twists are applied to the TSA simultaneously or in an arbitrary order. Future work on the coupling between voltage and twists would allow for a more robust model.

3.1.2 Polynomial Model

The polynomial model, given by the equation below, is used to predict the length of the string under a certain input (voltage, motor rotations, or electrical resistance).

$$L_{Poly}(q) = \sum_{i=0}^{k} p_i q^i, \tag{3.4}$$

where L_{poly} denotes the TSA's length predicted by the model. Depending on the experiment, q can be the input voltage V, the motor turns T, or electrical resistance R. The order of the polynomial is k and the coefficient of the i^{th} term is p_i. An order of $k = 3$ was chosen to model every relationship for low computational complexity and to prevent over-fitting. The coefficients of the polynomial are identified with the MATLAB function *polyfit*. The results of the polynomial model are compared to the Preisach models that account for hysteresis.

3.1.3 Evaluation Metrics

The performance of each model was evaluated using the average absolute error, E_{aver} and standard deviation, σ.

$$E_{\text{aver}} = \frac{1}{N}\sum_{i=1}^{N}|e_i|, \tag{3.5}$$

$$\sigma = \sqrt{\frac{1}{N-1}\sum_{i=1}^{N}(|e_i| - E_{\text{aver}})^2}, \tag{3.6}$$

where N is the number of evaluated data points and e_i is the error of the i^{th} data point.

3.1.4 Results

Preisach operators and polynomials captured the quasi-static relationship between input (twisting or heating) and output (length). Because each experiment applied two types of input to each actuator, each experiment required two distinct Preisach or polynomial models. For all Preisach models, the level of discretization, M, was chosen to be 20. Further increasing M did not generate appreciably better modeling results, but further increased the computational complexity of the model. The modeling results are summarized in Fig. 3.1(a). Polynomial coefficients for each loading condition, input mode, and string thickness are given in Table 3.1.

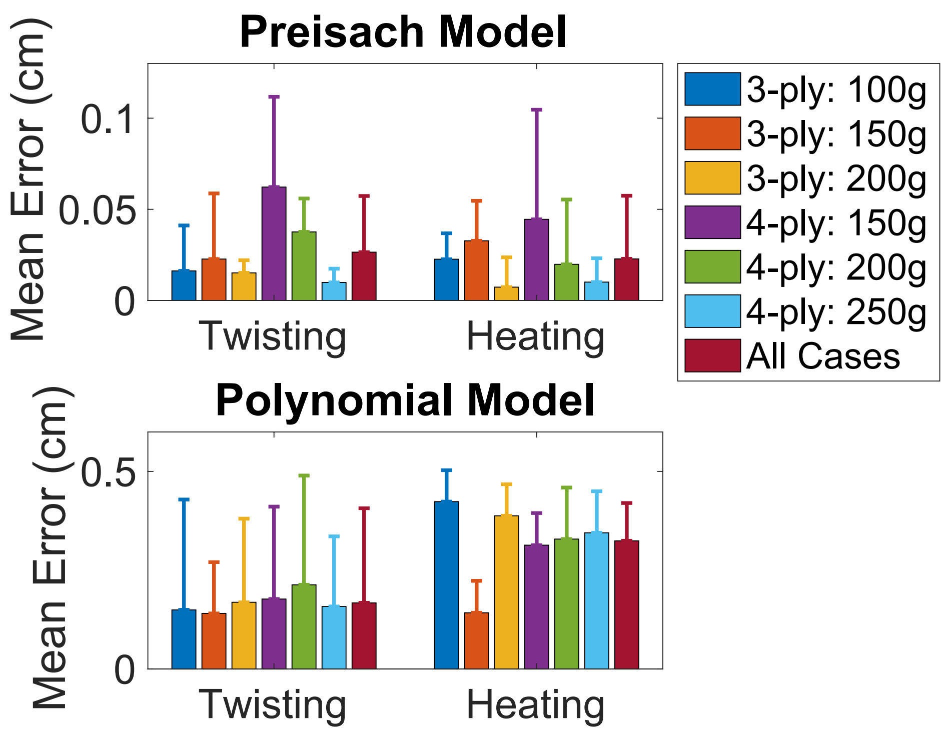

(a)

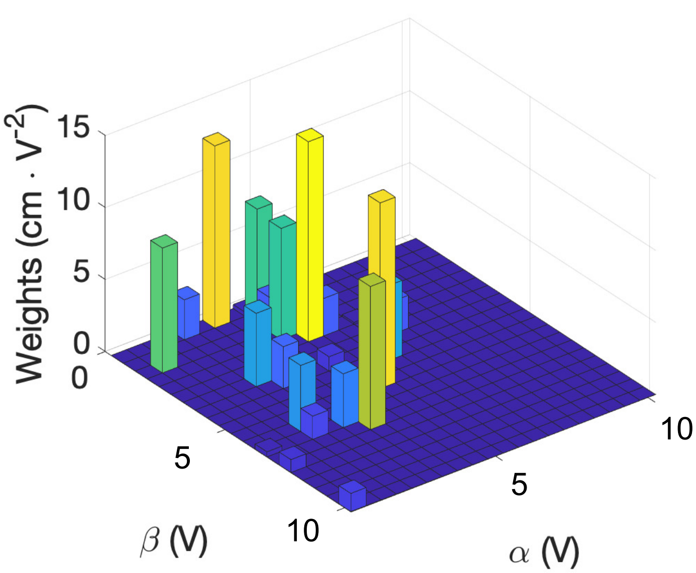

(b)

Figure 3.1: (a) The Preisach and polynomial modeling errors for SCP-based TSAs for twisting-induced and thermally-induced actuation. (b) An example of the Preisach density function for heated 3-ply strings under 100 g load.

Table 3.1: Identified parameters of the third-order polynomials for TSAs with twisting and heating inputs.

	p_0	p_1	p_2	p_3
3-ply (Twisting)				
100 g Load	28.54	-0.010	-0.001	0.000
150 g Load	30.01	-0.024	0.000	0.000
200 g Load	34.56	-0.029	0.000	0.000
4-ply (Twisting)				
150 g Load	28.48	-0.002	-0.001	0.000
200 g Load	30.93	-0.011	-0.001	0.000
250 g Load	32.32	-0.017	0.000	0.000
3-ply (Heating)				
100 g Load	23.69	-0.10	-0.08	0.008
150 g Load	25.71	0.32	-0.19	0.015
200 g Load	32.14	-0.32	-0.01	0.001
4-ply (Heating)				
150 g Load	23.94	0.673	-0.398	0.034
200 g Load	26.51	0.082	-0.184	0.016
250 g Load	31.68	-0.331	-0.046	0.004

Input Mode 1: Twisting

The average Preisach modeling error due to twisting for all cases was 0.0265±0.0346 cm. As seen in Fig. 3.1(a), the maximum average modeling error occurred for the condition of 4-ply strings with 150 g load at 0.0622±0.0601 cm. However, for all other cases, the average modeling errors were much less than 0.06 cm, which was extremely small compared to the mean length change of 3.927±0.845 cm due to twisting.

Third-order polynomials captured the relationship between length and twists reasonably well. Fig. 3.1(a) shows that for every loading condition, the average error was no more than 0.2131±0.1304 cm. Considering all string thicknesses and loading conditions, the average polynomial modeling error was 0.1673±0.0956 cm. The polynomial models had average errors more than six times larger than that of the Preisach hysteresis models in TSAs with twisting as the input mode. Much of the modeling error was because the polynomial model did not capture the hysteresis in the SCP strings. The coefficient of the third-order term, p_3 was computed to have an absolute value of less than $4.1 \times 10^{-6}\text{cm}/\Omega^3$ for all loading conditions and both string thicknesses (ply numbers) when twisting was the input mode. This meant the strain could have been modeled through a second-order polynomial. Geometry-based models derived for stiff-string TSAs in the literature are also second-order [32].

Input Model 2: Heating

The thermally-induced actuation demonstrated the benefit of the Preisach hysteresis model over third-order polynomial models. Although the modeling error varied over different cases, the Preisach modeling error of all heated and twisted strings averaged 0.0228 ± 0.0308 cm and 0.0265 ± 0.0346 cm, respectively (Fig. 3.1(a)). Since the average overall length change from heating was 3.117 ± 0.863 cm, the Preisach model accurately captured the actuation behavior. As an example, the discretized weights u_{ij} are shown in Fig. 3.1(b) for heated 3-ply strings under 100 g load. As shown, most of the weight terms are located outside of diagonal regions, which describe the significance of the hysteresis [78].

Using third-order polynomial models, the mean modeling error for heated strings was greater than that of twisted strings, as shown in Fig. 3.1(a). The thermally-induced actuation (length–voltage) showed more significant hysteresis than the twisting-induced actuation (length–twisting). Although second-order polynomials were sufficient to capture the twisting-induced actuation, the thermally-induced actuation required the third-order term, p_3. Table 3.1 shows p_i for the heated strings. The third-order terms are quite low. The greatest value of p_3 was $0.034\,\mathrm{cm}/\Omega^3$, which was obtained for 4-ply strings under 150 g load. The lowest value of p_3 was only $0.001\,\mathrm{cm}/\Omega^3$, which was obtained for for 3-ply strings under 200 g load. The value of p_0 increased as the applied load increased for both 3-ply and 4-ply strings. This was because the low stiffness of the SCP strings made their lengths increase significantly as the applied load increased.

3.2 Modeling of TSA Self-Sensing

3.2.1 Quasi-static Modeling

Similar to actuation, self-sensing during twisting was captured by a Preisach operator with different parameter values. The equation for the relationship between electrical resistance and length is given below:

$$L_{\text{Preisach}}(R) = \sum_{i=1}^{M} \sum_{j=1}^{M+1-i} \xi_{ij} z_{ij}(R) + b_R, \tag{3.7}$$

where R is the electrical resistance and obtained experimentally. b_R is a constant offset. The discretized weight is ξ_{ij} and z_{ij} depends fully on the experimentally obtained resistance history. The identification of the Preisach model was worked out as a linear least-squares problem and solved with the MATLAB function *lsqnonneg*. The Preisach model is explained in more detail in previous studies [73, 79, 80].

Preisach models and third-order polynomials captured the relationship between resistance and length for different self-sensing schemes with different loading conditions and string thicknesses. A summary of results is provided in Fig. 3.2(a). The resistance values were taken as inputs to predict the lengths of the TSAs. For all self-sensing models, the discretization level M of the Preisach operator was chosen to be 20. The typical discretized weights ξ_{ij} in the hysteresis models are shown in Fig. 3.2(b). As shown, the major weights are mostly located in the diagonal region, which is responsible for describing the hysteresis-free correlation [78] — the twisting-induced hysteresis is less evident. All loading conditions and string thicknesses are captured by the model.

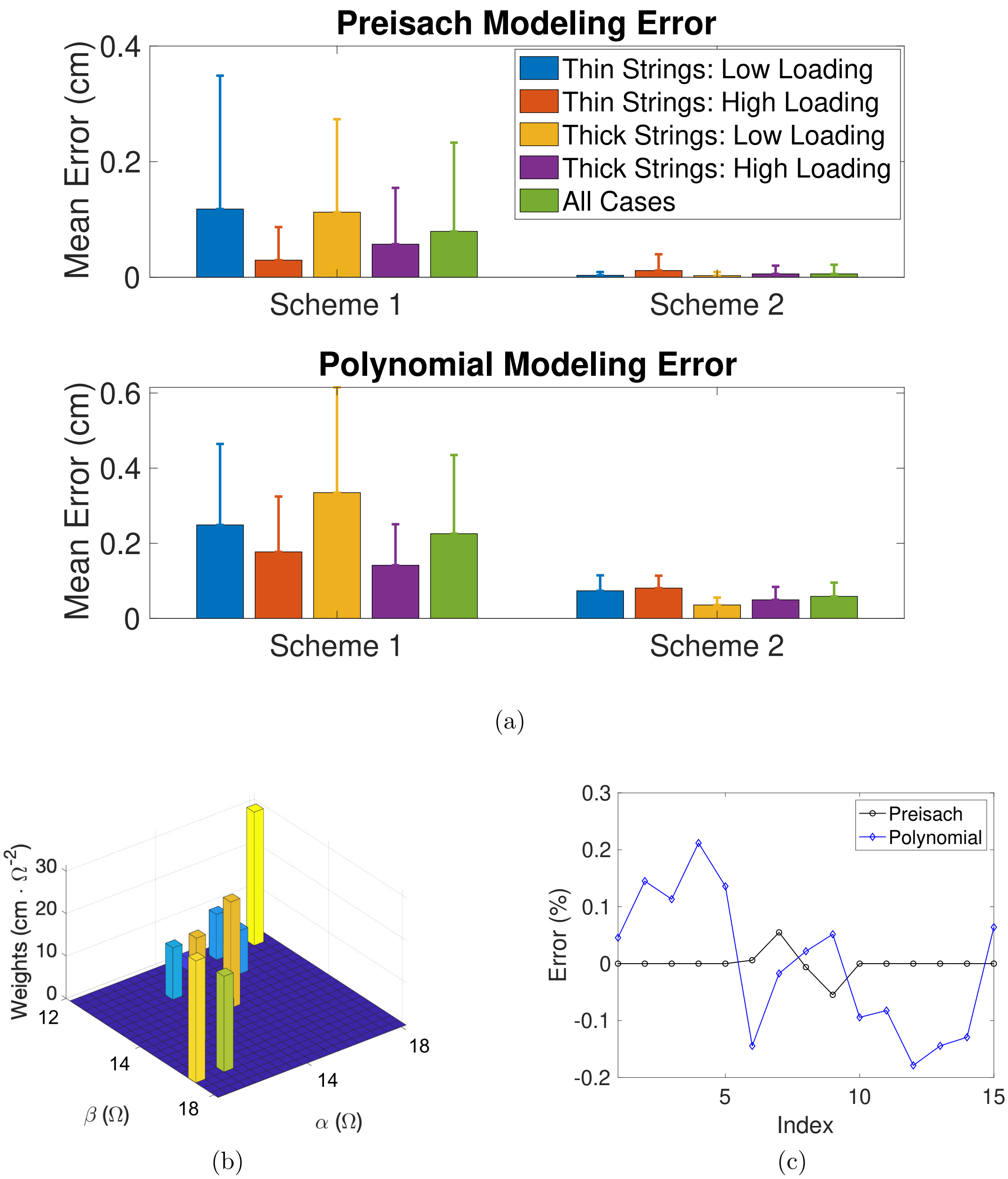

Figure 3.2: (a) The Preisach and polynomial modeling errors for SCP-based TSAs for self-sensing during twisting based on the resistance measurement. (b) An example of the identified Preisach weights for *Scheme 2* with thin strings and attached 250 g mass. (c) An example of the modeling error percentage from the Preisach and polynomial models for *Scheme 2* with thick strings and attached 700 g mass.

Self-sensing models were realized only during twisting-induced actuation in this study due to the potential coupling between resistance and temperature during thermal actuation. For that reason, thermal actuation is recommended only when large actuation is required, because of three main reasons below.

1. It is challenging to ensure the uniform temperature of the proposed actuator during thermal actuation.
2. The thermal model of this proposed actuator has not yet been studied.
3. Self-sensing during thermal actuation may depend on many factors, such as actuator temperature, ambient temperature, airflow, and humidity.

Previous studies showed that the temperature of a single SCP actuator during thermal actuation was highly non-uniform [81]. The proposed actuator in this study was more complicated because it was composed of two SCP actuators twisted about each other, with each Joule-heated via a conductive silver coating. The thermal properties of individual SCP actuators have been studied [11], but for our proposed actuator, behaviors such as time constants during heating/cooling and voltage-temperature correlations have not yet been studied. The potential coupling between resistance and temperature was also indicated by the stress-deformation responses of a single SCP actuator at various temperatures [82].

The polynomial coefficients for the self-sensing experiments are provided in Table 3.2. The modeling results are shown in Fig. 3.2(a). *Scheme 1* had a greater modeling error than *Scheme 2* for every string thickness and loading condition. That behavior occurred for both polynomial and Preisach hysteresis models. In particular, the TSAs of *Scheme 2* with 8-ply SCPs and high loading had the least amount of polynomial modeling error, which indicated a relatively low amount of hysteresis (Fig. 3.2(a)).

Although modeling errors were larger for *Scheme 1* on average, the TSAs in *Scheme 1* also had a larger range of contraction.

Table 3.2: Identified parameters of the third-order polynomials for the self-sensing behavior in TSAs.

	p_0	p_1	p_2	p_3
Scheme 1, Case 1				
450 g Load	-506.75	62.87	-2.49	0.0330
550 g Load	-443.20	53.80	-2.07	0.0268
Scheme 1, Case 2				
700 g Load	-170.84	39.14	-2.52	0.0544
900 g Load	-72.34	17.62	-0.99	0.0187
Scheme 2, Case 1				
250 g Load	-40.54	12.63	-0.73	0.0148
350 g Load	-81.32	20.41	-1.22	0.0246
Scheme 2, Case 2				
700 g Load	-21.36	16.66	-1.73	0.0625
900 g Load	-5.98	11.13	-1.03	0.0337

For all loading conditions and thicknesses, the average Preisach modeling error was 0.0793±0.1536 cm for *Scheme 1.* Strings with lower loading had greater Preisach modeling error than strings with higher loading, similar to when polynomial models were utilized.

Third-order polynomials had an average modeling error of 0.2256±0.2093 cm for all loading conditions and string thicknesses, as shown in Fig. 3.2(a). The average overall length change for this self-sensing scheme was 6.947±0.808 cm. For *Scheme 1*, thin and thick strings had less polynomial modeling error at the greater loading conditions (350 g for thin strings and 900 g for thick strings).

The average Preisach modeling error was extremely low for *Scheme 2* at only 0.0057±0.0159 cm for all strings with different values of thickness and under different loading conditions. On average, the overall length change of the TSA was 2.673±0.251 cm. This average length change was less than half that of *Scheme 1*. Thin strings with high loading had the most modeling error, at 0.0115±0.0282 cm. The lowest modeling error occurred for thick strings with low loading, at 0.0027±0.0063 cm. An example of the modeling errors from Preisach and polynomial models is given in Fig. 3.2(c), in this case for two SCP strings with 700 g attached. "Index" is the numbering of quasi-static length values. In Fig. 3.2(c), the modeling error is displayed as a percentage of the measured length, which changes slightly for each index.

The average polynomial modeling error for *Scheme 2* was 0.0588±0.0366 cm, approximately one-fourth of the average polynomial modeling error of strings in *Scheme 1*. At high and low loading conditions, thick (8-ply) strings had less modeling error than thin (4-ply) strings, as shown in Fig. 3.2(a). *Scheme 1* and *Scheme 2* had, on average, comparable modeling error percentages, since *Scheme 2* had less absolute modeling error but a smaller contraction range.

3.2.2 Transient Modeling

The proposed model to capture the strain-resistance relation was a sum of transient decay, hysteresis, and creep components. After the model was identified, its inversion was used as the self-sensing model to estimate strain based on resistance. This procedure was convenient since the resistance of the SCP strings not only depended on the strain generated by the TSA but also on time, as the TSA exhibited transient decay and creep.

Derivation: Strain–Resistance Model

The resistance of the TSA, y_{model}, can be expressed as the sum of three terms, namely, transient decay, hysteresis, and creep. The overall resistance y_{model} is written as follows:

$$y_{model} = y_t + y_h + y_c, \tag{3.8}$$

where y_t is the transient response of the resistance, y_h is the hysteresis term, and y_c is the creep term. The response not due to transient decay, y_s, is modeled with the sum of the resistance due to hysteresis y_h and creep y_c: $y_{s,model} = y_h + y_c = y_{model} - y_t$. The formula is additive due to a precedent in an existing study on creep and hysteresis in piezoelectric actuators [76].

Transient Decay: While the TSA was at rest (the motor was not rotating), the resistance decayed at a decreasing rate. This behavior is shown in Fig. 2.8(b). Experiments showed that the length instantly reached its steady-state after each rotation of the motor. Therefore, the transient resistance decay did not have a corresponding length decay or increase. It is proposed that the overall resistance is expressed by

$$y_{model}(t) = b_1 \ln^2(t - t_0 + \varepsilon) + b_2 \ln(t - t_0 + \varepsilon) + y_{s,model}, \tag{3.9}$$

where t_0 is the instant when the motor stops rotating and $t > t_0$, $y_{s,model}$ is the resistance value when $t - t_0 = 1$, $b_1 < 0$ and $b_2 < 0$ are constants to be identified and they are constrained to be negative due to the resistance decay. ε is a small positive constant. When $t = t_0$, there will be a singularity in the natural logarithms. In order to avoid the singularity, a small offset of $\varepsilon = 1 \times 10^{-5}\,\mathrm{s}$ was added. Note that this model of transient decay is not physics-based, but was selected for its ability to highly accurately capture the transient length–resistance correlation. Note y_s, the response not due to transient decay, is estimated by the hysteresis term and creep term to be $y_{s,model}$. Therefore, the transient decay y_t is defined as $y_t = b_1 \ln^2(t - t_0 + \varepsilon) + b_2 \ln(t - t_0 + \varepsilon)$.

A decaying exponential function was also attempted to model the transient decay. However, it was found that the approach required different b_1 and b_2 values for each set of experiments with a specific step duration, making it difficult to obtain a generalized model. Therefore, Eq. (3.9) was adopted in this study where b_1 and b_2 take the same values for all sets of experiments with different step durations.

Hysteresis: A rate-dependent Prandtl-Ishlinskii (PI) model [83, 75] was adopted to capture the hysteresis component of the strain-resistance relationship, to incorporate the motor step input duration that affects the peak-to-peak value of the resistance, as shown in Fig. 2.8(a). The PI model was chosen over other existing hysteresis models because model inversion will be required for self-sensing and the analytical inversion of the PI model can be efficiently obtained [76]. The output y_h of the PI model is a weighted sum of play operators with different thresholds. The play operator, $F_r[v](t)$, is described as follows:

$$\begin{aligned} F_r[v](0) &= f_r(v(0), 0) = w(0), \\ F_r[v](t) &= f_r(v(t), F_r[v](t_i)),\ \forall t_i \leq t \leq t_{i+1}, \\ f_r(v, w) &= \max(v - r, \min(v + r, w)),\ w = F_r[v](t_i), \end{aligned} \tag{3.10}$$

where v is the input, t_i and t_{i+1} are the time indices, and r is the threshold. The output of the discretized PI model is written as follows:

$$y_h = \sum_{n=1}^{N_h} p(r_n) F_{r_n}[v](k), \tag{3.11}$$

where N_h is the number of play operators used in the model, $p(r_n)$ are the densities, and k is the discrete-time index. For the rate-dependent PI model, the threshold is described as a function of the rate of change of input $\dot{v}$. In this work, $\dot{v}$ was defined as the division of length step-size by the step duration. The threshold r is described as

$$r = \alpha \ln(\beta + \lambda |\dot{v}(t)|^{\epsilon}), \tag{3.12}$$

where α, β are positive constants. This modeling scheme was proven to be effective in the existing literature [83]. The densities p_n, λ, and ϵ are identified with a least-squares optimization approach. For more details on the PI hysteresis model, readers are directed to [76, 83].

Creep: The creep was modeled as a weighted summation of several creep operators plus a term proportional to the input. A discrete version of the creep operator was adopted as follows:

$$x_i(k) = e^{-\Lambda_i T} x_i(k-1) + (1 - e^{-\Lambda_i T}) v(k-1), \tag{3.13}$$

where x_i is the creep operator, v is the input, $\Lambda_i > 0$ for $i = 1, 2, ..., N_c$, and T is the sampling time [76]. N_c is the order of the creep model. Using Eq. (3.13), the output of the creep model y_c is described in Eq. (3.14):

$$y_c = \sum_{i=1}^{N_c} c_i x_i(k) + a v_i, \tag{3.14}$$

where c_i are the densities and a is a constant. The densities and the constant are identified as a least-squares optimization problem. Other ways to model creep in smart materials could also be used [84].

Derivation: Self-Sensing Model

The PI model is analytically invertible and the inverse is another PI model [76]. Therefore, the length L of the TSA is efficiently obtained as follows:

$$L[u](k) = \bar{a}u(k) + \sum_{i=1}^{N_H} \bar{w}_i F_{\bar{r}_i}[u](k), \tag{3.15}$$

where $u(k)$ is defined as follows:

$$u(k) = y_{exp}[L](k) - y_c(k) - y_t(k). \tag{3.16}$$

Subtracting the creep and transient terms from the resistance measurements yields the hysteresis term. Because the value of $y_c(k)$ depends only on the previous value of the length, it can therefore be computed without knowing the current value of the length. y_t does not depend on the length. The parameters $\bar{a}$, w_i, and $\bar{r}_i$ are computed directly from the previously identified parameters of the PI model [76]. The output of the play operator $F_{\bar{r}_i}(k)$ depends on the thresholds $\bar{r}_i$ as follows:

$$F_{\bar{r}_i}(k) = \begin{cases} \min(o_2(u(k)) + \bar{r}_i, F_{\bar{r}_i}(k-1)), & u(k) < u(k-1) \\ \max(o_1(u(k)) - \bar{r}_i, F_{\bar{r}_i}(k-1)), & u(k) > u(k-1) \\ F_{\bar{r}_i}(k-1), & u(k) = u(k-1), \end{cases} \tag{3.17}$$

where o_1 and o_2 are envelope functions given below expressed with hyperbolic tangents, as given in [75]:

$$\begin{aligned} o_1(u(k)) &= \rho_0 \tanh(\rho_1 u(k) + \rho_2) + \rho_3, \\ o_2(u(k)) &= \phi_0 \tanh(\phi_1 u(k) + \phi_2) + \phi_3, \end{aligned} \tag{3.18}$$

where ρ_0, ρ_1, ρ_2, ρ_3 and ϕ_0, ϕ_1, ϕ_2, ϕ_3 are constant parameters to be identified.

Procedure

The proposed model was identified based on two sets of experiments with step durations of 6 s and 32 s. The model was then validated on three sets of experiments with step durations of 2.4 s, 17 s, and 98 s. The model was identified with the following procedure:

1. Construct an $m \times n$ matrix that contains the experimental resistance values, where m is the number of transient curves and n is the number of sampled points in each transient curve.

2. Obtain an equation of fit for the transient decay y_t, by passing each row of the matrix into a curve fitting function. A second-order polynomial relationship between $\ln(t - t_0)$ and transient resistance y_t was identified with the MATLAB function *polyfit*.

3. Store the m values of $y_s = y_{exp} - y_t$ into a separate vector. y_s will be the input to the creep and hysteresis model.

4. Initialize a vector X, whose elements are the model parameters to identify. Let $y_{s,model}(X)$ be an $m \times 1$ vector that denotes the output of the model due to the parameters contained in X. In this study, a nonlinear multivariable function, $f(X)$, was formulated such that:

$$f(X) = \sum_{k=1}^{m} \left(y_{s,model,k}(X) - y_{s,k} \right)^2. \tag{3.19}$$

   By utilizing the MATLAB function *fmincon*, the optimal constrained parameters were identified when $f(X)$ reached a local minimum. The iterative computation stops when the function stops decreasing to within a specified tolerance and specified constraints are satisfied with the specified tolerance as well. If the local minimum yields an error larger than a given threshold, rerun the optimization with different starting values for X to obtain a different local minimum. The interior-point algorithm was utilized [85], but other algorithms may also be used.

5. Obtain the strain-resistance model as follows:

$$y_{model}(k) = y_{s,model}(k) + y_t(k). \tag{3.20}$$

6. Finally, the self-sensing model is obtained through inversion of the strain-resistance model. The input to the self-sensing rate-dependent PI model is $u(k)$ from Eq. (3.16). There are eight additional parameters to identify: ρ_0, ρ_1, ρ_2, ρ_3, ϕ_0, ϕ_1, ϕ_2, and ϕ_3 from Eq. (3.18). To solve for these parameters, utilize the same strategy from the previous step to minimize the sum of squared differences between the actual and modeled lengths.

Identification

An order of $N_c = 2$ and $N_h = 60$ was chosen for the creep model and hysteresis model, respectively. Further increasing either N_c or N_h negligibly decreased modeling error but increased the computational complexity. The experimental measurements with 6s and 32s motor input step durations were used to identify the model. For the strain-resistance model, the initial value of X was chosen to contain each element equal to one for an initial value of $f(X) = 1.44{\times}10^5\,\Omega^2$. The function converged after 267 iterations of $f(X)$, where each iteration decreased $f(X)$. After optimization, the final value of $f(X)$ was $3.42{\times}10^{-2}\,\Omega^2$. Similarly, for the self-sensing model, X was initialized such that all model parameters equaled one for an initial value of $f(X) = 9.50{\times}10^1\,\text{cm}^2$, and the function converged after 35 iterations to a final value of $f(X) = 2.13\,\text{cm}^2$. Other initial parameter values can also be used. The key model parameters are provided in Table 3.3. Although the function $f(X)$ is highly nonlinear and may have many local minima, the low modeling errors in the next section suggested the parameter identification was satisfactory. Furthermore, it was found that the model parameters were identified to be similar under different initial conditions.

Table 3.3: Identified Model Parameters

Strain-Resistance Model		Self-Sensing Model	
Parameter	Value	Parameter	Value
Λ_1	1.27×10^{-2}	ρ_0	1.25×10^3
Λ_2	9.61×10^{-1}	ρ_1	1.68×10^3
c_1	-5.20×10^2 Ω/cm	ρ_2	1.68×10^3
c_2	526.1 Ω/cm	ρ_3	1.25×10^3
a	-1407.3 Ω/cm	ϕ_0	1.15×10^3
b_1	-1.71×10^{-3} Ω	ϕ_1	1.68×10^3
b_2	-2.68×10^{-2} Ω	ϕ_2	1.68×10^3
		ϕ_3	2.21×10^3

For each sampled point, the error E_i of the i^{th} point is defined as the absolute value of the difference between the experimental and modeled results, as given below:

$$\begin{aligned} E_{i,\text{strain-resistance}} &= \frac{|y_{\text{i,model}} - y_{\text{i,exp}}|}{y_{\text{i,exp}}} \times 100\%, \\ E_{i,\text{self-sensing}} &= \frac{|L_{\text{i,model}} - L_{\text{i,exp}}|}{L_{\text{i,exp}}} \times 100\%. \end{aligned} \tag{3.21}$$

The strain-resistance model identification results are shown in Fig. 3.3(a)–(b) for the cases with 6 s and 32 s step durations. Similarly, the self-sensing model identification results are shown in 3.3(c)–(d) respectively. The average strain-resistance modeling errors for the 6 s and 32 s step durations were $0.19\% \times y_{exp}$ (0.0104 Ω) and $0.29\% \times y_{exp}$ (0.0164 Ω), respectively. The maximum strain-resistance modeling identification error was $0.94\% \times y_{exp}$ (0.054Ω). Similarly, the average self-sensing modeling errors were respectively $0.090\% \times L_{exp}$ (0.0226 cm) and $0.092\% \times L_{exp}$ (0.0239 cm) for the cases with 6 s and 32 s step durations. The maximum self-sensing modeling identification error was $0.30\% \times L_{exp}$ (0.0691 cm).

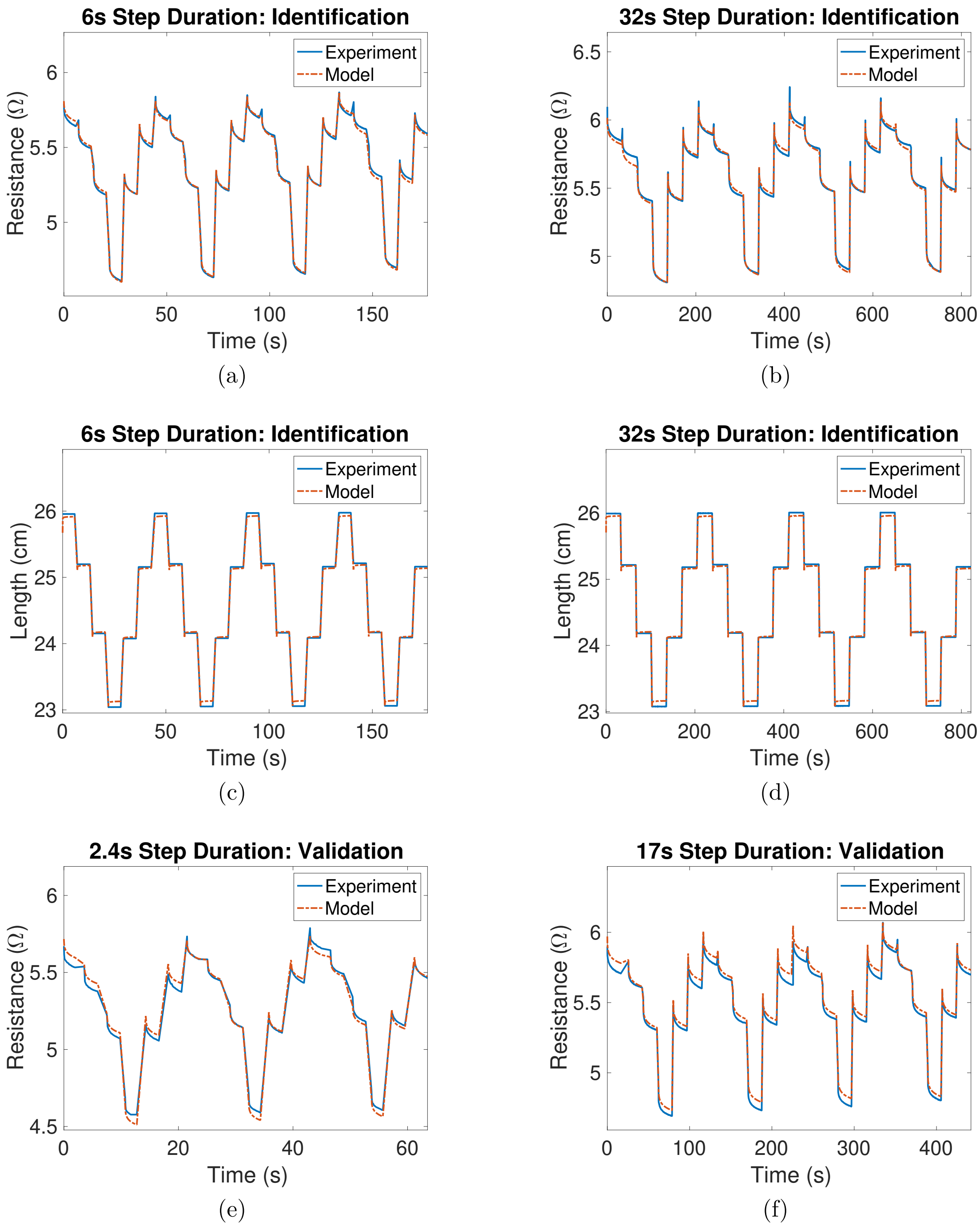

Figure 3.3: Strain-resistance model identification results for (a) 6 s and (b) 32 s step durations. Self-sensing model identification results for (c) 6 s and (d) 32 s step durations. Strain-resistance model validation results for (e) 2.4 s and (f) 17 s.

Validation

Using the previously identified parameters, the model was validated on experimental measurements with 2.4 s, 17 s, and 98 s step durations. The strain-resistance model validation results are shown in Fig. 3.3(e), 3.3(f), and 3.4(a) respectively for the cases with 2.4 s, 17 s, and 98 s step durations. Similarly, the corresponding self-sensing model validation results are shown in Fig. 3.4(b), (c), and (d) respectively. The average strain-resistance modeling errors for the cases with 2.4 s, 17 s, and 98 s step durations were $0.58\% \times y_{exp}$ ($0.0283\ \Omega$), $0.65\% \times y_{exp}$ ($0.0349\ \Omega$), and $0.55\% \times y_{exp}$ ($0.0303\ \Omega$), respectively. The maximum strain-resistance model validation error was $1.63\% \times y_{exp}$ (0.106Ω). Similarly, the average self-sensing modeling errors were $0.086\% \times L_{exp}$ (0.0213 cm), $0.14\% \times L_{exp}$ (0.0352 cm), and $0.12\% \times L_{exp}$ (0.0308 cm) for the cases with 2.4 s, 17 s, and 98 s step durations, respectively. The maximum self-sensing modeling validation error was $0.46\% \times L_{exp}$ (0.1196 cm).

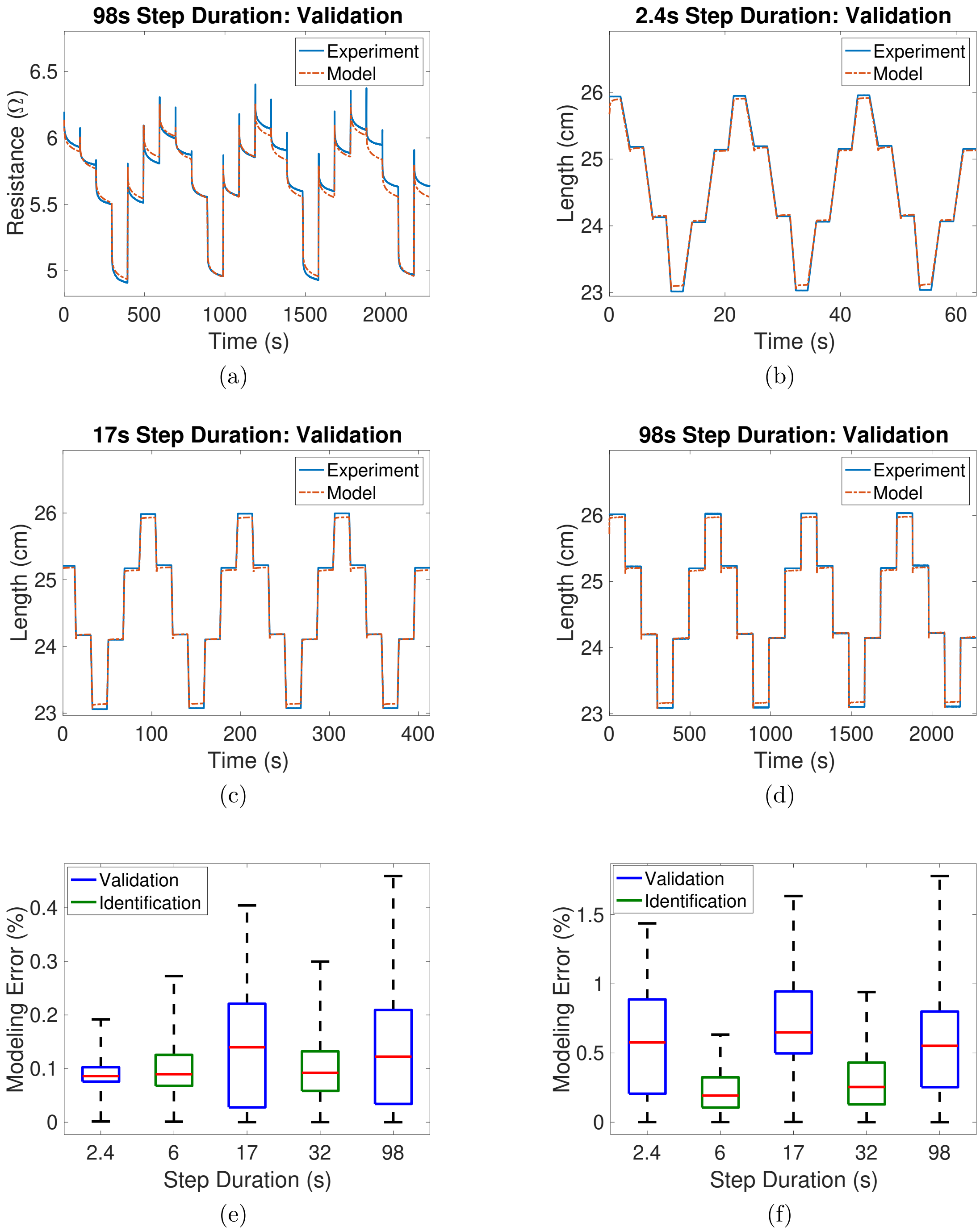

Figure 3.4: Strain-resistance model validation results for (a) 98 s step durations. Self-sensing modeling validation results for (b) 2.4 s, (c) 17 s, and (d) 98 s step durations. A summary of the modeling error percentages for all step durations in (e) self-sensing model and (f) strain-resistance model.

The overall performances of the self-sensing model and strain-resistance model are provided in Fig. 3.4(e) and 3.4(f), respectively. The model validation error was slightly greater than the identification error. The proposed self-sensing model with a single set of parameters worked for all cases with different twisting steps and step durations. The motor rotations need not be measured, as long as the load remains constant and the string twists stay within the working range of the TSA. It must be known whether the motor is on or off, as this determines whether or not the resistance transiently decays.

CHAPTER 4
TSA-DRIVEN SOFT ROBOTS

For this chapter, three TSA-driven robots were developed. Firstly, a three-fingered gripper was developed, with each finger driven by a pair of antagonistic TSAs [63]. Next, a soft robotic manipulator was developed [86]. Lastly, an anthropomorphic soft gripper was developed. The antagonistic TSA configuration was studied in previous work [61], thus only design and fabrication for the compliant gripper were completed. The TSA-driven soft manipulator required a novel modeling strategy based on the properties of the TSA and the geometry of the manipulator. For that reason, the design, fabrication, characterization, and modeling of the manipulator were completed. The anthropomorphic soft gripper's fingers were designed like the soft manipulator. Therefore, only the fabrication and grasping demonstrations for the anthropomorphic gripper were completed.

4.1 Three-Fingered Compliant Gripper

The SCP-based TSAs were applied to a robotic gripper (Fig. 4.1). Consisting of three robotic fingers, it was designed to gently, yet securely, grip objects. Each finger was designed based on a modified version of the Fin Ray® Effect [60], where applied force to the side of the structure caused it to bend inward to the object for improved grip. Each finger also contained a rigid "spine" that allowed inward bending but restricted backward bending. This feature was advantageous for grasping heavy objects whose weight would have otherwise caused the fingers to bend backwards. Each TSA enabled high output forces with less input torque than simply a spool of string on a motor shaft [31]. The motors, located near the bottom of the gripper, were attached to strings connected pulleys that rotated the fingers (Fig. 4.1(b)). Small motors kept the gripper's mass low. The base of the gripper was cylindrical in order to attach to the end of a rigid robotic arm.

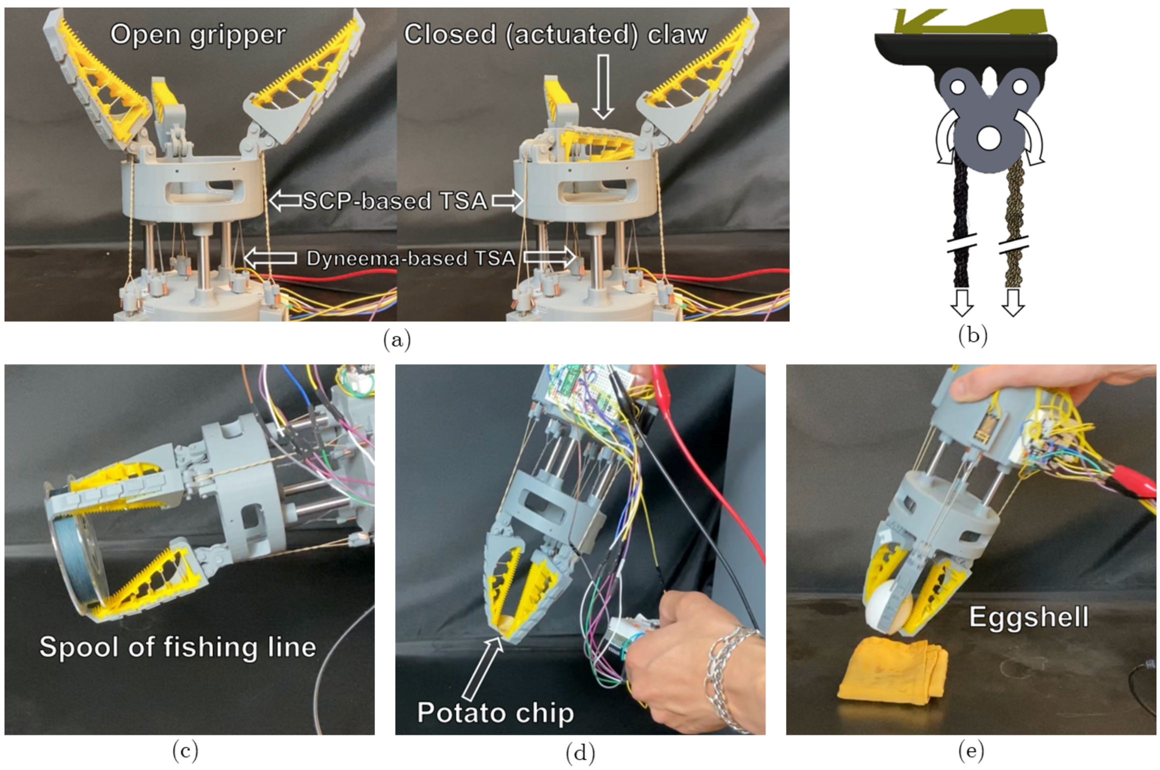

Figure 4.1: (a) The gripper's finger in the open and closed configuration. (b) The antagonistic configuration of the two TSAs attached to a hinge that rotated the finger. The gripper gently grasped various objects, such as (c) a spool of fishing line, (d) a potato chip, and (e) an eggshell.

For each finger, two TSAs were connected in an antagonistic configuration. One of the TSAs consisted of two SCP strings, while the other TSA consisted of two UHMWPE strings. The contraction of the UHMWPE-based TSA pulled the finger inward. Meanwhile, the SCP-based TSA stretched and provided an opposing force. The contraction of the SCP-based TSA and untwisting of the UHMWPE-based TSA pulled the finger outward. Inexpensive 3D-printed and off-the-shelf parts keep the cost low. The robot was constructed for less than $100, with most of the cost coming from the electric motors. No specialized equipment was used to make the robot, except for a commercially-available fused-deposition-modeling (FDM) 3D printer (Zortrax M200).

Mechanical components were mostly 3D printed, whereas electrical components were inexpensive yet with a high degree of flexibility in application. The individual fingers were made from flexible 3D-printed thermoplastic polyurethane (TPU), while the base was 3D-printed with rigid acrylonitrile butadiene styrene (ABS) plastic. In Fig. 4.1, the ABS and TPU are shown in gray and yellow, respectively. For gripping small objects, each finger also possessed rigid "fingernails" made from ABS plastic. Each finger was controlled by two small DC motors, for a total of six motors in the gripper. A 16 MHz microcontroller based on the ATmega328P microchip controlled the six motors through three Polulu DRV8835 motor drivers. Push buttons turned the motors on or off in either the forward or reverse direction. Each motor had a no-load speed of 590 RPM and a stall torque of 960 g·cm. In addition, each motor had a mass of only 9.5 g, which helped the mass of the overall robot remain low.

The current iteration of the robot successfully grasped objects of various sizes, shapes, and masses. Fig. 4.1(c)–(e) shows the gripper holding a spool of fishing line, potato chip, and eggshell. These objects had masses of approximately 100 g, 2 g, and 6 g, respectively. When only one finger was actuated, it had a maximum rotation angle of approximately 120°. If all three fingers were simultaneously actuated, each finger had a maximum rotation angle of approximately 55°. The compliance of both the SCP strings and TPU enabled safe human-robot interaction and handling of delicate objects. Compliance could have been achieved with compliant rubber cords or a soft spring in series with stiff strings. However, one advantage of the proposed actuation technology in this work is that the opposing force to the Dyneema-based TSA can be actively varied by heating and twisting the SCP-based TSA. Another advantage is that self-sensing may be achieved by measuring the resistance of the SCP-based TSA.

When the finger was not actuated (both TSAs were fully untwisted), the resistance was 20.3 Ω. When the finger was rotated fully inward, the SCP string was found to have a resistance of 26.9 Ω. When the finger rotated inward, the SCP string stretched and its resistance consequently increased. Future work will include the control of the gripper based on self-sensing strain feedback. One possible future application of this type of robot is in food processing facilities, where the robot must safely interact with delicate food items. Although heat may be generated to power the proposed TSA, the strain can be generated to the end-effector over a distance. The gripper showcases the benefits of using compliant and large-strain TSAs with promising self-sensing potential during twisting-induced and thermally-induced actuation.

4.2 Soft-Bodied Manipulator

This section presents design, fabrication, and kinematic models which predict the single-DOF behavior of the soft robotic manipulator powered by TSAs. Unlike previous models which are based on either numerical methods or solid mechanics [22], the proposed models utilized TSA kinematics and provided analytical solutions that enabled further insight into the manipulator's performance. Firstly, design and fabrication of the soft manipulator was completed. Next, a physics-based model to capture the single-DOF kinematic behavior of the soft manipulator was derived. The model, which was developed by considering the strain kinematics of the TSAs, provided analytical solutions to predict the pose of the manipulator. Secondly, the velocity kinematics of the manipulator were studied. For this purpose, the equations provided by the bending angle model and the TSA velocity equations were utilized.

4.2.1 Design and Fabrication

The design of the soft arm used three TSAs in conjunction to bend and orient the endpoint of the manipulator in multiple directions. The natural compliance of the soft robot allowed for safe human-robot interaction. The soft arm, as shown in Fig. 4.2(a), was constructed from Smooth-On Ecoflex™00-50 silicone via a 3D printed mold. The mold was designed to be printed quickly and be disposable. The walls of each mold part were 0.8-mm thick—twice the nozzle diameter of the 3D printer—to optimize slicing and printing. The thin walls also allowed for the model to be quickly broken apart to retrieve the cast arm. The soft arm was 175-mm long and utilized three internal channels to house the TSAs' strings. The channels were placed evenly at angles 120° from each other near the circumference of the arm. A channel was also provided in the center of the arm that contained the wires of the inertial measurement unit (IMU). The fabricated robot is shown in Fig. 4.2(b).

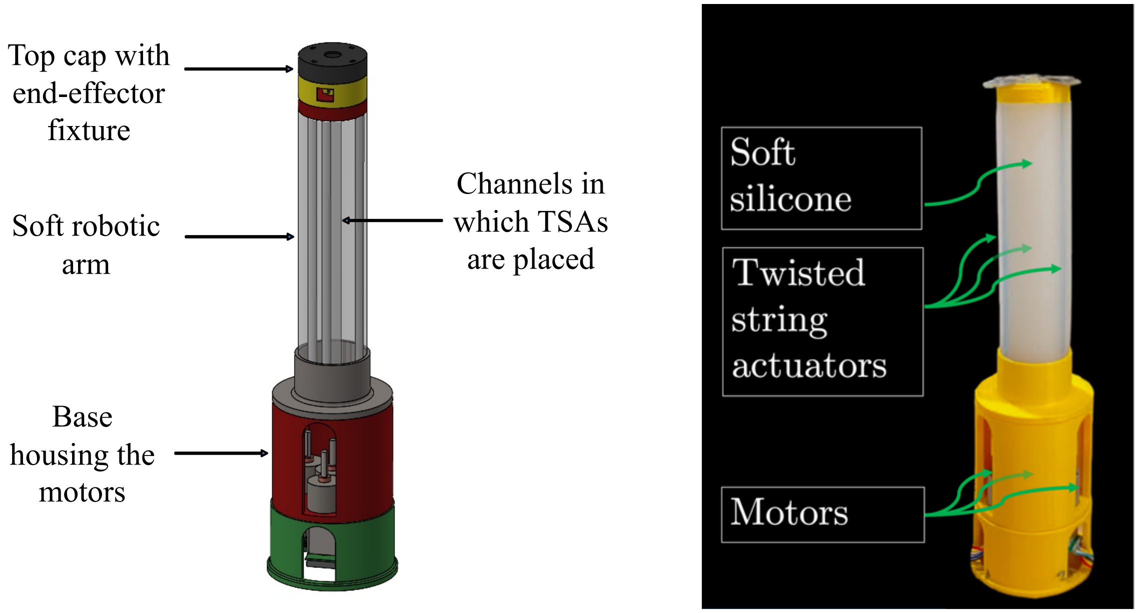

(a) (b)

Figure 4.2: (a) Model of the soft arm. (b) Photograph after fabrication.

The soft arm utilized three TSAs to enable bending in all directions, thereby providing the robot with multiple DOF. The arm functioned by actuating the TSAs, where each TSA could be actuated at varying levels in conjunction with one another to bend in any direction in the range of the TSA pair. The bending angle of the arm was varied by varying the twists in any TSA. The base of the arm housed the motors to actuate the TSAs and encoders to measure the number of twists. The electronics were placed outside of the robot and were wired to the motors and encoders. The three elements of the base section were also designed using a peg-and-slot system to be printed separately and efficiently, reducing support material, printing time, and printing cost. Leading up to the arm, the topmost base section utilized friction to grip the outer diameter of the arm so that it did not fall off of the base. The axial forces exerted by the TSAs fixed the arm to the base.

The top caps, where the ends of the TSAs attached, were attached to the silicone both by friction (by following the inner diameter of the center channel) and axial force of the twisted strings. Additionally, the simple design of the end piece could allow for any type of end-effector to be attached. All rigid parts of the arm were 3D printed on a traditional FDM printer from ABS plastic.

This study utilized two strings with the same length and material properties to construct each TSA. More strings with different material properties could also have been used [32]. The strings were hung vertically in tension with one end attached to the motor shaft. The free end of the strings was attached to the top cap of the arm and was constrained such that the arm bent due to the motor's rotation. More information on the design and assembly of TSAs can be found in [32]. The TSAs were realized using UHMWPE strings with diameters of 1.0 mm. This material and diameter were chosen due to their repeated usage in previous studies [32]. Brushed DC motors (Metal Gearmotor 20Dx44L, Pololu) with a 125:1 gear ratio twisted the pairs of strings to realize the TSAs. Each DC motor utilized a dual-channel Hall-effect sensor board to track the motor rotations. Accounting for the gear ratio, the encoders enabled 625 counts per revolution (CPR). 625 CPR corresponded to 0.58°-resolution sensing of the angle of the motor output shaft. With a 12-V input, each motor was able to output 7.8 kg·cm of torque before stalling, but each motor had a mass of only 46 g. A microcontroller based on the ATmega2560 microchip (MEGA 2560 R3 Board, Elegoo) with brushed DC motor drivers (DRV8871, Adafruit) controlled the robot.

An absolute orientation sensor (VR IMU Breakout - BNO080, Sparkfun) was used to measure the bending angle of the soft TSA-driven arm. The IMU returned the orientation in terms of quaternions which were converted into the roll, pitch, and yaw angles (Euler angles) for modeling purposes.

4.2.2 Kinematic Modeling

Bending Angle

The diagram of the robot is provided in Fig. 4.3. The model relied on the following assumptions:

1. The robot bent with a curvature radius R that was uniform along the entire center arc length L_0.
2. The center arc length of the silicone, L_0, was constant during bending.
3. The TSAs that were not twisted experienced negligible tension.
4. The length X_0 of the untwisted TSA equaled the height L_0 of the unbent manipulator. Similarly, the twisted length X of the TSA equaled the arc length L of the bent robot.
5. The stiffness of the strings was considered to be great enough such that, within the range of tested loads, the axial force on the TSA alone caused a negligible strain in the TSA.

Assumptions #1 and #2 were previously used in studies on soft robotics [87, 12, 6]. Assumption #3 permitted an acceptably low modeling error in this study. Assumption #4 was valid due to the locations of the motors relative to the silicone. Assumption #5 was due to the high stiffness of the strings. The stiffness of a single 1.3-mm UHMWPE string was measured to be 662 N, normalized to a unit length of 1 m. The maximum force on a TSA was 16.27 N in this study.

Let θ be the bending angle of the robot in radians. The arc length L is

$$L = \theta(R - r), \tag{4.1}$$

where R is the center radius of curvature, and r is the distance between the center of the soft silicone arm and the TSA's strings (Fig. 4.3). As shown in Fig. 4.3, r is not the radius of the soft silicone itself, which was slightly larger than r. $d = 3.25\,\text{mm}$ is the difference between the silicone's radius and r, but its value does not affect the analysis. The center arc length $L_0 = \theta R$ can be rearranged as

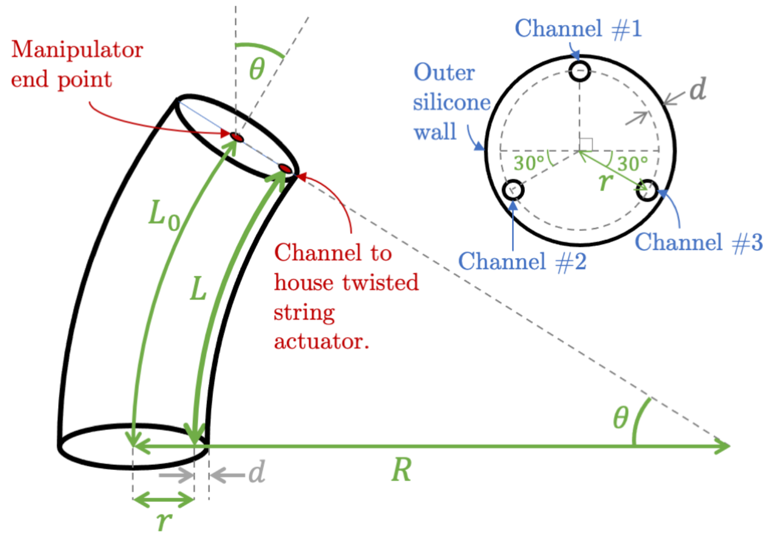

Figure 4.3: The diagram of the soft robot actuated by TSAs, with relevant variables labeled. From the top view of the robot, the motors are placed 120° apart.

$$R = \frac{L_0}{\theta}, \tag{4.2}$$

where L_0 is a constant and is the arc length of the robot when it is not bent. During bending, L decreased because the axial forces exerted by the TSA compressed the silicone body. Substituting Eq. (4.2) into Eq. (4.1) yields

$$L = L_0 - \theta r. \tag{4.3}$$

As derived in previous studies [32, 31], the kinetostatic model of the TSA is given by

$$X = \sqrt{X_0^2 - T^2 w^2}, \tag{4.4}$$

where X is the length of the TSA's strings and X_0 is the initial (untwisted) length of the TSA's strings. Considering the robot's structure, we can assume that $L = X$ and $X_0 = L_0$. T is the angle of the motor's shaft in radians and w is the variable radius of the TSA. Consistent with existing studies, Eq. (4.4) does not have a stiffness term [31, 32].

According to [32], the variable radius w of the TSA is given by

$$w = w_0 \sqrt{\frac{L_0}{L}}, \tag{4.5}$$

where w_0 is the radius of the string when it is untwisted [31]. In practice, w_0 is measured with a caliper. The design of the robotic manipulator restricts L from direct measurement. Furthermore, L and w depend on each other. This requires L to be estimated based on the previous estimate of w, such that

$$L[k] = \sqrt{L_0^2 - T[k]^2 w[k-1]^2}, \tag{4.6}$$

where k is the discrete time index, $w[0] = w_0$, and $T[1] = 0$. $w[k]$ is then computed using Eq. (4.5) and Eq. (4.6) as follows:

$$w[k] = w_0 \sqrt{\frac{L_0}{\sqrt{L_0^2 - T[k]^2 w[k-1]^2}}}, \tag{4.7}$$

Considering $L = X$ and $L_0 = X_0$, equating the right-hand sides of Eq. (4.3) and Eq. (4.4), and then solving for θ yields

$$\theta = \frac{L_0 - L}{r} = \frac{L_0 - \sqrt{L_0^2 - T^2 w^2}}{r}. \tag{4.8}$$

Angular Velocity

In this study, three different models of $\dot{\theta}$ are proposed. The characteristics of these models are stated below:

- The "complete model" accounts for $\dot{w}$, the estimated rate of change in the TSA's radius.
- The "conventional model" approximates that $\dot{w} = 0$.
- The "linearized model" simplifies the conventional model by approximating L as a linear function of T.

Complete Model: As reported in [32], differentiating Eq. (4.8) with respect to time yields

$$\dot{\theta} = \frac{\left(\dot{T}w + T\dot{w}\right) Tw}{r\sqrt{L_0^2 - T^2w^2}}. \tag{4.9}$$

Eq. (4.9) is hereby named the "complete model" because it accounts for $\dot{w}$. The derivation for $\dot{w}$ is as follows. By differentiating Eq. (4.5), and using Eq. (4.4) with the assumptions that $L = X$ and $L_0 = X_0$, the following equation is derived:

$$\dot{w} = \frac{1}{2} w_0 L_0^{1/2} L^{-5/2} Tw(T\dot{w} + \dot{T}w). \tag{4.10}$$

By rearranging terms and solving for $\dot{w}$,

$$\dot{w} = \frac{w_0 L_0^{1/2} Tw^2}{2L^{5/2} - w_0 L_0^{1/2} wT^2}\dot{T}. \tag{4.11}$$

Conventional Model: In many previous studies on TSAs, $\dot{w}$ was assumed to be negligible [37, 31, 88]. In that case,

$$\dot{\theta} = \left(\frac{1}{r}\frac{dL}{dT}\right)\dot{T} = \left(\frac{1}{r}\frac{w^2T}{\sqrt{L_0^2 - w^2T^2}}\right)\dot{T}. \tag{4.12}$$

The quantity $\frac{dL}{dT}$ is known as the "generalized reduction ratio" and denoted by $h(T)$ [88, 31]. Although $h(T)$ also depends on w, w is implicitly a function of T. Therefore, $h(T)$ is ultimately a function of T only. Other studies referred to $\frac{dL}{dT}$ as the "TSA Jacobian"[37, 89]. This thesis uses the term "generalized reduction ratio" over "TSA Jacobian" to avoid confusion with the overall system Jacobian $\mathcal{J}$. If a constant radius of the TSA is assumed, the Jacobian of the overall system is

$$\mathcal{J} = \frac{h(T)}{r}, \tag{4.13}$$

where

$$\dot{\theta} = \mathcal{J}\dot{T}. \tag{4.14}$$

Equation Eq. (4.14) is just another way to express Eq. (4.12).

Linearized Model: By rearranging Eq. (4.4) and consistent with [32, 31], the following relationship is obtained for the TSA:

$$T^2w^2 + L^2 - {L_0}^2 = 0. \tag{4.15}$$

By differentiating Eq. (4.15) with respect to time, the following relationship is obtained:

$$T\dot{T}w^2 - L\dot{L} = 0, \tag{4.16}$$

where $\dot{w}$ and $\dot{L}_0$ are assumed to be negligible relative to $\dot{T}$ and $\dot{L}$. This is because L_0 is constant, and due to the TSA's high stiffness, $\dot{w}$ is approximated to be 0. Solving for $\dot{L}$, the linear velocity of the TSA, yields

$$\dot{L} = \frac{dL}{dT}\dot{T} = \frac{w^2T}{L}\dot{T}. \tag{4.17}$$

$\frac{dL}{dT}$ defines the generalized reduction ratio,

$$h(T) = \frac{dL}{dT} = \frac{w^2T}{L} = \frac{w^2T}{\sqrt{L_0^2 - T^2w^2}}. \tag{4.18}$$

The generalized gear reduction was also necessary for the dynamic model of the system to translate a desired length of the TSA into the desired motor rotation angle. A useful approximation can be derived if one notes that

$$\left.\frac{dh}{dT}\right|_{T=0} = \left.\frac{w^2}{\sqrt{L_0^2 - T^2 w^2}}\right|_{T=0} = \frac{w^2}{L_0}, \tag{4.19}$$

and

$$\left.\frac{d^2h}{dT^2}\right|_{T=0} = \left.\frac{Tw^4}{2(L_0^2 - T^2 w^2)^{\frac{3}{2}}}\right|_{T=0} = 0. \tag{4.20}$$

Now using the Taylor Series expansion at $T = 0$ (also known as the Maclaurin Series expansion), a second-order approximation of $h(T)$ can be calculated. Since the Taylor Series expansion was centered at $T = 0$,

$$h(T)|_{T\approx 0} = \left.\frac{w^2 T}{\sqrt{L_0^2 - T^2 w^2}}\right|_{T\approx 0} = \frac{w^2}{L_0}T + \mathcal{O}(T^3). \tag{4.21}$$

This defines linearization of the generalized gear reduction $\tilde{h}$ and linearization of the system Jacobian $\tilde{\mathcal{J}}$ when $T \approx 0$, respectively:

$$\tilde{h}(T) = \frac{w^2}{L_0}T,\ \tilde{\mathcal{J}} = \frac{\tilde{h}(T)}{r} = \frac{w^2}{rL_0}T. \tag{4.22}$$

In this linear region, Eq. (4.14) can be simplified to

$$\dot{\theta} = \tilde{\mathcal{J}}\dot{T} = \frac{w^2 T}{rL_0}\dot{T}. \tag{4.23}$$

Eq. (4.23) is the linearized model.

4.2.3 Experimental Results

Experimental Characterization

The input sequence for this experimental characterization is provided in Fig. 4.4(a). The motor rotations were applied in monotonically increasing, then monotonically decreasing steps for four complete cycles. These number of cycles were selected to examine the repeatability of the soft manipulator. The motor was actuated in steps of 1 rotation and paused for 2 s to ensure the motor angle and bending angle became steady. The motor angle (twists) varied between 3 and 18 revolutions (rev). The initial offset of 3 rev was introduced to the motor to ensure the actuating strings were taut. However, this offset was not applied for the other (non-actuating) motors to ensure that they did not exert significant force to oppose the motion of the manipulator. Because TSAs require tension to actuate, this offset had a negligible effect on the initial bending angle of the manipulator.

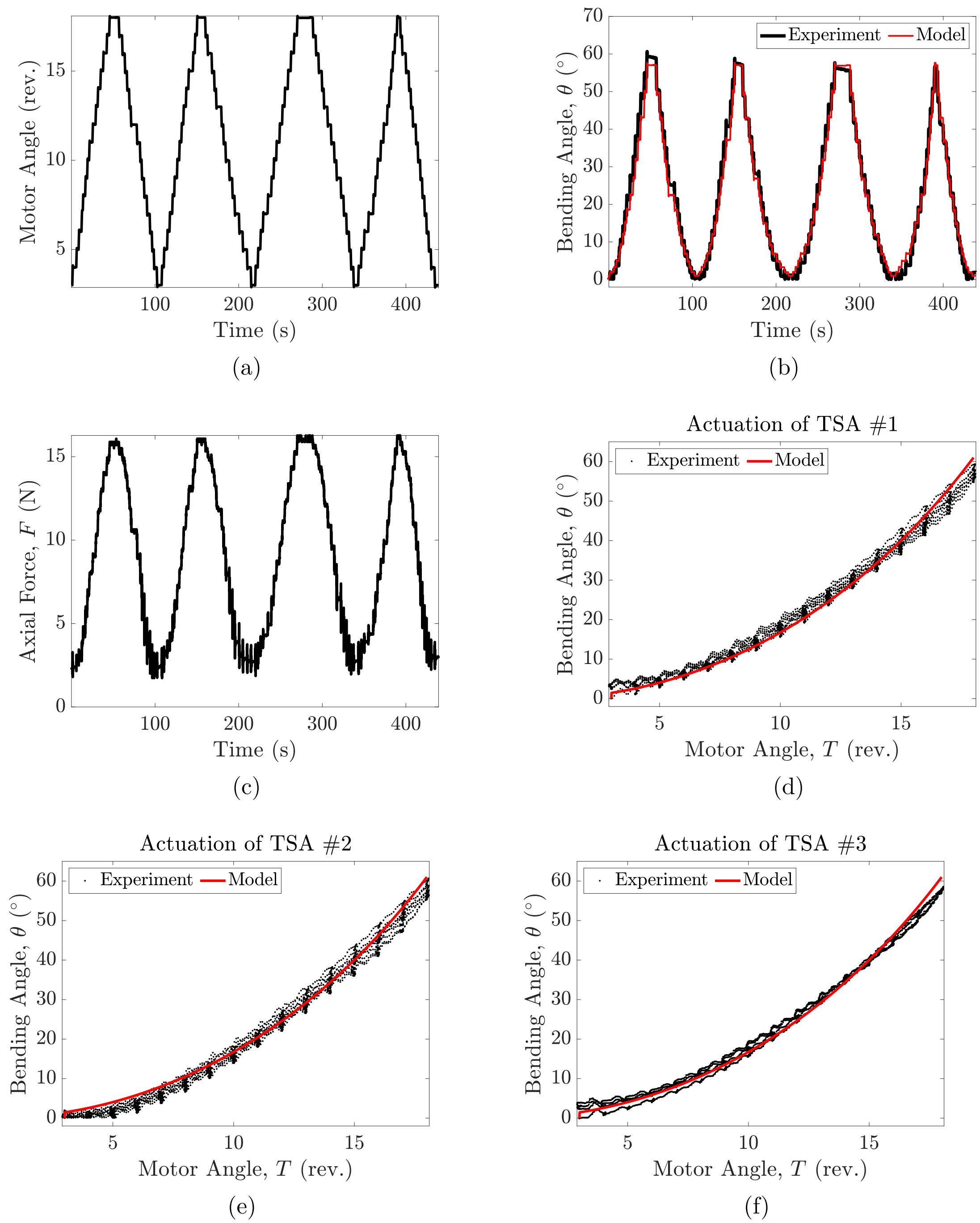

Figure 4.4: Experimental characterization and kinematic modeling results. As an example, the results from the actuation of TSA #2 are presented in (a)–(c). (a) Applied motor angle T input sequence versus time t. (b) Experimental and modeled bending angle θ versus t. (c) Axial force F versus t. Experimental and modeled θ versus T for (d) TSA #1, (e) TSA #2, and (f) TSA #3.

The experimental characterization was performed for all three TSAs. As an example, the results of TSA #2 are shown. The bending angle θ and axial force F versus time are shown in Fig. 4.4(b) and 4.4(c), respectively. The bending angle was measured about the axis normal to the actuating motor shaft. Mild hysteresis was observed in both the bending angle–motor turns, and the axial force–motor turns correlations, which was consistent with previous work [32]. As shown in Fig. 4.4(c), the axial force F exerted by the manipulator on the TSA was measured using force-sensitive resistors (FSR-404, Interlink Electronics). An initial force of 1.73 N kept the strings taut, and F increased as θ increased. At 18 motor rotations, the TSA exerted an axial force of 16.27 N. At low motor angles, small oscillations in θ caused corresponding oscillations in F. As θ increased, the oscillations in F disappeared because the silicone was stiffened.

Modeling Results

The model between turns and bending angle in Eq. (4.8) was experimentally validated for the three TSAs employed in the manipulator. The values of L_0, r, and w_0 were measured to be 0.175 m, 1.675×10^{-2} m, and 6.5×10^{-4} m, respectively. As an example, the modeling results of bending angle due to TSA #2 are presented as a function of time in Fig. 4.4(b). As seen from the results in Fig. 4.4(c)–4.4(f), the experimental results of the bending due to the three TSAs agreed well with the derived model. The modeling error was computed as follows. Firstly, the error in the model was computed for each TSA using the equation $E_i[k] = |\theta_{i,\text{exp}}[k] - \theta_{i,\text{model}}[k]|$, where $E_i[k]$ is the error of the k^{th} point of the i^{th} TSA. $\theta_{i,\text{exp}}$ and $\theta_{i,\text{model}}$ are respectively the experimentally-obtained and modeled bending angle for the i^{th} TSA. Secondly, by utilizing the errors computed for each TSA, the weighted average error was computed using the following equations:

$$\overline{E}_i = \frac{1}{n_i}\sum_{k=1}^{n_i} E_i[k], \quad \widehat{E} = \frac{1}{m}\sum_{i=1}^{m} \overline{E_i}, \tag{4.24}$$

where $\overline{E}_\mathrm{i}$ is the mean error in the bending angle model for the i^{th} TSA, n_i is the number of values in the data set for the i^{th} TSA, $m = 3$ is the number of TSAs, and $\widehat{E}$ is the weighted average error of the model. The error between the experimental results and the model is presented in Fig. 4.5(a). The weighted average modeling error was found to be $\widehat{E} = 1.58°$, which was considered to be acceptable because the range of bending angle was approximately 60°. For TSAs #1, #2, and #3, $\overline{E}_1 = 1.36°$, $\overline{E}_2 = 1.68°$, and $\overline{E}_3 = 1.71°$, respectively.

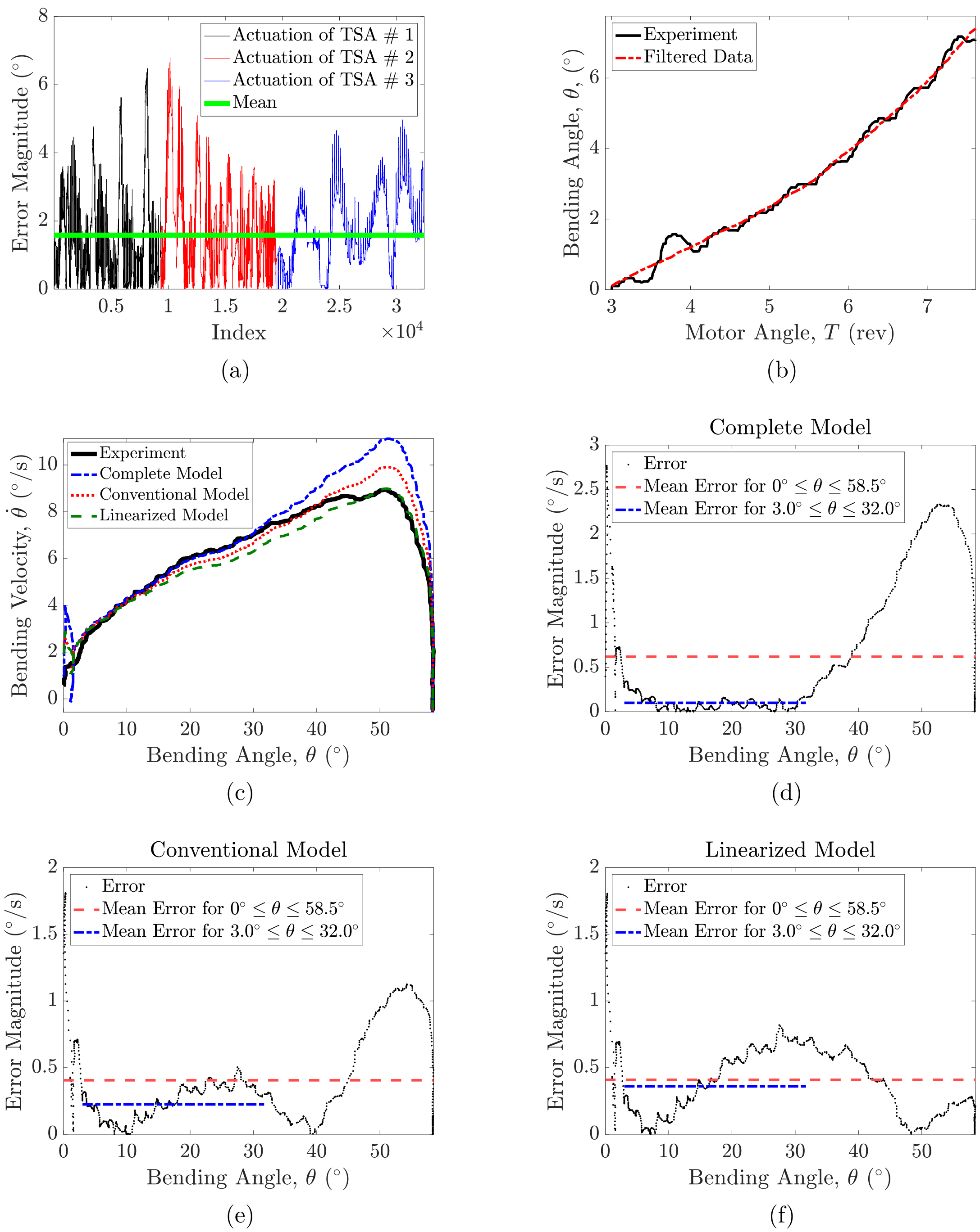

Figure 4.5: (a) Modeling error magnitude. (b)–(f): Velocity modeling results. (b) Raw and filtered θ versus T. (c) Experimental bending velocity $\dot{\theta}$ versus $\theta[T]$ compared to three different models. Error magnitude from the (d) complete model, (e) conventional model, and (f) linearized model.

The model between the angular velocity of the motor shaft $\dot{T}$ and the bending angular velocity $\dot{\theta}$ was validated through experiments. For this experiment, a step input voltage of 3.6 V was applied to the motor for 14 s, after which the input voltage dropped to 0 V. The motor reached a steady-state velocity of 1.90 rev/s. A third-order Savitsky-Golay filter [90] with a window size of 151 samples taken at 53.9 Hz differentiated T to obtain $\dot{T}$, θ to obtain $\dot{\theta}$, and w to obtain $\dot{w}$. The parameters of the filter were selected such that a significant amount of noise was eliminated while a negligible amount of bending information was lost. As an example, the raw versus filtered θ values are shown in Fig. 4.5(b). This filter was used to determine $\dot{w}$ instead of Eq. (4.11) because $\dot{w}$ was highly sensitive to the measurements of w_0 and L_0.

To model the correlation between $\dot{T}$ and $\dot{\theta}$, three different models were tested: the complete model, the conventional model, and the linearized model. The experimental data and modeling results for each strategy are shown in Fig. 4.5(c). At $\theta \leq 3°$, the experimental results significantly disagreed with the models. This disagreement was likely because the actuated TSA was slightly loose in the initial twisting stage. At $\theta \geq 40°$, the complete model and conventional model significantly overestimated $\dot{\theta}$. This overestimation may be due to Assumption #3: the tensions in the non-actuated strings were not trivial, which could slow the bending of the manipulator and lead to a smaller $\dot{\theta}$ than expected.

Within the range of $3° \leq \theta \leq 32°$, the complete model clearly performed the best. The errors for the complete, conventional, and linearized models are shown in Fig. 4.5(d), 4.5(e), and 4.5(f), respectively. The error was computed using $|\dot{\theta}_{i,\mathrm{exp}}[k] - \dot{\theta}_{i,\mathrm{model}}[k]|$. In this range, the mean error in the complete model was only 0.100°/s. The conventional model and linearized model had errors of 0.224°/s and 0.356°/s, respectively when $3° \leq \theta \leq 32°$. However, when $0° \leq \theta \leq 58.5°$, the performance of the complete model decreased. When $0° \leq \theta \leq 58.5°$, the complete model had the greatest mean error (0.619°/s) but the least median error (0.226°/s). The conventional model experienced similar spikes in error as the complete model. It had a mean error of 0.405°/s and median error of 0.287°/s when $0° \leq \theta \leq 58.5°$. In comparison, the error spikes in the linearized model were less drastic. Its mean error was 0.409°/s and its median error was 0.292°/s for $0° \leq \theta \leq 58.5°$.

4.2.4 Control

A closed-loop proportional control strategy was developed to obtain desired bending angles of the arm. The speeds of the motors were adjusted by varying the duty cycles of pulse-width modulated (PWM) 12-V signals. The input voltage V_m to the motor was bounded such that $2.4\,\mathrm{V} < V_m < 12\,\mathrm{V}$. The upper bound was the nominal voltage of the motor that was provided by the manufacturer. The lower bound was the minimum voltage at which the motor produced sufficient torque to twist the TSA's strings and bend the robot's body. In addition, a control board was fabricated to independently actuate each motor using push buttons and to set the motors' speeds using four potentiometers. Two buttons each corresponded to each of the four motors: one button spun the motor clockwise whereas the other button spun the motor counterclockwise. In closed-loop control, the bending angle of the arm was measured by the orientation sensor to directly obtain the error between the desired bending angle and the actual bending angle. This error was utilized to determine the control input. The duty cycle of V_m was proportional to the bending angle error. The proportional gain, $K_p = 5$, was determined experimentally. The lower bound of 2.4 V meant that, even when K decreased, the input voltage to the motor remained at 2.4 V for $|T - T_{\text{des}}| < 10°$. $K \leq 5$ prevented the overshoot of the motor rotation angle. The steady-state closed-loop control performance is shown in Fig. 4.6(a). The experimental procedure consisted of step reference signals whose amplitudes were uniformly-distributed random floating-point numbers in the range of $[0°, 60°]$. The control error was defined as

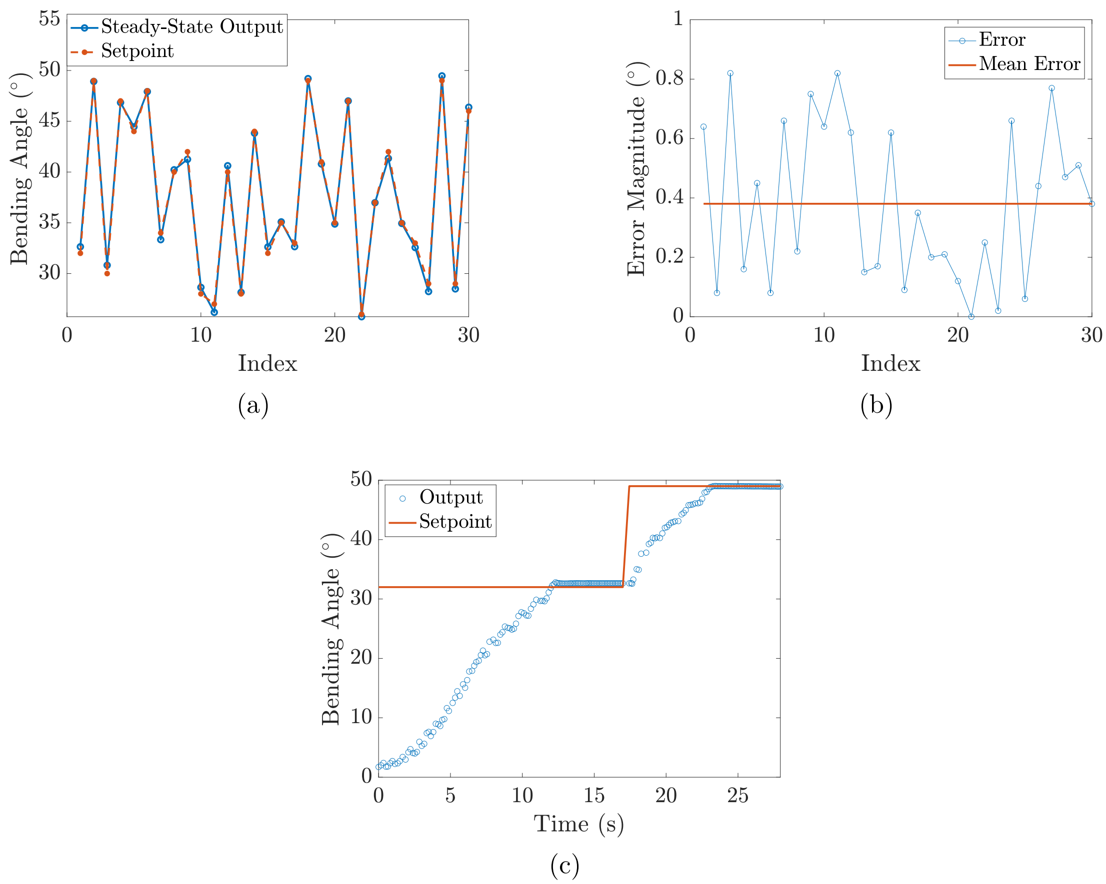

Figure 4.6: The control performance of the TSA-driven soft robot. (a) The setpoint and steady-state error of the closed-loop bending angle controller and (b) corresponding steady-state error. (c) The step-response of the bending angle with closed-loop control for two different setpoints.

$$E_k = |T_{k,\mathrm{exp}} - T_{k,\mathrm{des}}|, \tag{4.25}$$

where E_k is the error of the k^{th} point. T_{exp} and T_{des} are respectively the experimentally-obtained and desired outputs of the system. The error magnitude of the controller is shown in Fig. 4.6(b), in which the maximum and average errors were 0.82°and 0.38°, respectively.

The step response of the closed-loop system for two different step reference signals is shown in Fig. 4.6(c). The rise time t_r for a desired bending angle $T_{des} = 32°$ was $t_r = 8.03\,\mathrm{s}$. t_r was defined as the time in which the bending angle of the arm changed from 10% to 90% of T_{des}. The rise time could be decreased by (1) using a motor with a lower gear ratio, or (2) using strings with larger diameters. Decreasing the gear ratio would increase the angular speed of the motor without increasing the size or mass of the motor, but the motor's smaller torque output may decrease the maximum bending angle. Although larger-diameter strings would increase the contraction speed of the TSA, the minimum required torque from the motor would also increase, as shown in the model developed by [37]. Because the motors mostly operated at the saturation voltage, increasing K_p may not significantly decrease the rise time.

4.3 Anthropomorphic Soft Gripper

Many other types of soft robots can be made from TSAs. In addition to the manipulator and three-fingered gripper, a standalone anthropomorphic soft-robotic gripper with tendon-based stiffening was developed using TSAs (Fig. 4.7). The hand consisted of four fingers and a thumb. The TSAs enable six independently controllable motions—one for each of the four fingers and two for the thumb. Each finger bent due to the contraction of its corresponding TSA, whereas the thumb can both bend and roll using two TSAs. It is widely reported that the thumb is responsible for more than 50% of a human hand's gripping capabilities [91, 92]. Therefore, the 2-DOF thumb was very beneficial to allow the gripper to replicate more anthropomorphic grasps and perform in-hand manipulation. As shown in Fig. 4.7, the gripper was capable of both dexterous and strong grasps. Each finger possessed two TSAs, as shown in Fig. 4.7. One TSA was primarily used to bend the finger, whereas the other TSA was used to stiffen the finger by opposing the force due to the primary TSA.

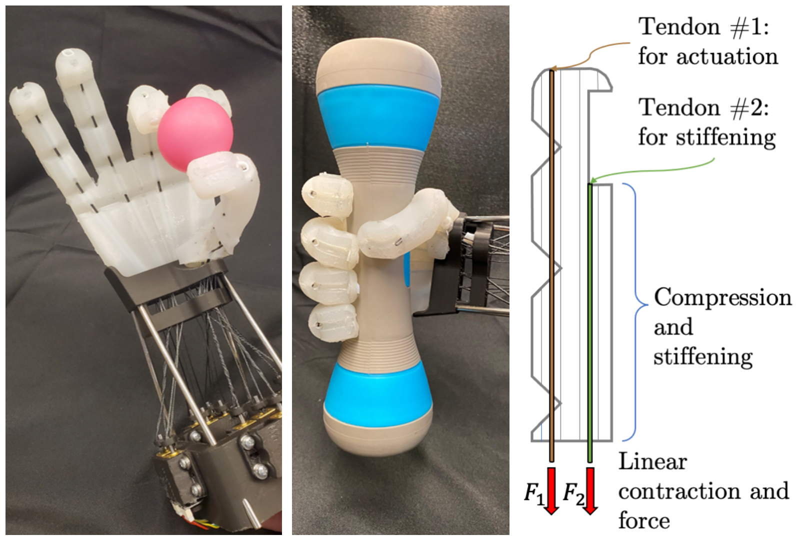

Figure 4.7: The anthropomorphic soft robotic gripper driven by TSAs. (left) An example of the gripper's precision grasping and (center) power grasping. (right) The gripper is also capable of tendon-based stiffening via an antagonistic TSA. By actuating both TSAs in the finger, the silicone will compress and stiffen. The bending angle of the gripper is determined by the net bending moment due to F_1 and F_2.

The performance of the gripper was analyzed by replicating a variety of anthropomorphic grasps according to the Feix GRASP taxonomy presented in [1]. This taxonomy has been widely used to demonstrate the dexterity of a gripper under consideration. The results achieved by the proposed gripper are presented in Fig. 4.8. The proposed gripper achieved 31 of the 33 grasps presented [1]. The gripper failed to achieve the parallel extension grasp (grasp #22); the best effort is shown in Fig. 4.8. To achieve this grasp, the fingers and thumb needed to actuate from their bases to clamp an object while remaining extended. However, due to the pseudo joints in the proposed finger design, the bending was uniformly distributed across the length of the finger. This feature made it nearly impossible for the gripper to achieve the proximal bending concentration required for the parallel grasp. This can potentially be addressed by employing fingers that do not use pseudo joints or adding a second DOF in each finger to allow decoupled proximal bending. Furthermore, for the adduction grip (grasp #23), the gripper was only able to hold on to the object through passive force and not using a controllable DOF. Enabling this actuation can be addressed in the next iteration of the gripper by adding a controllable DOF in the palm of the gripper.

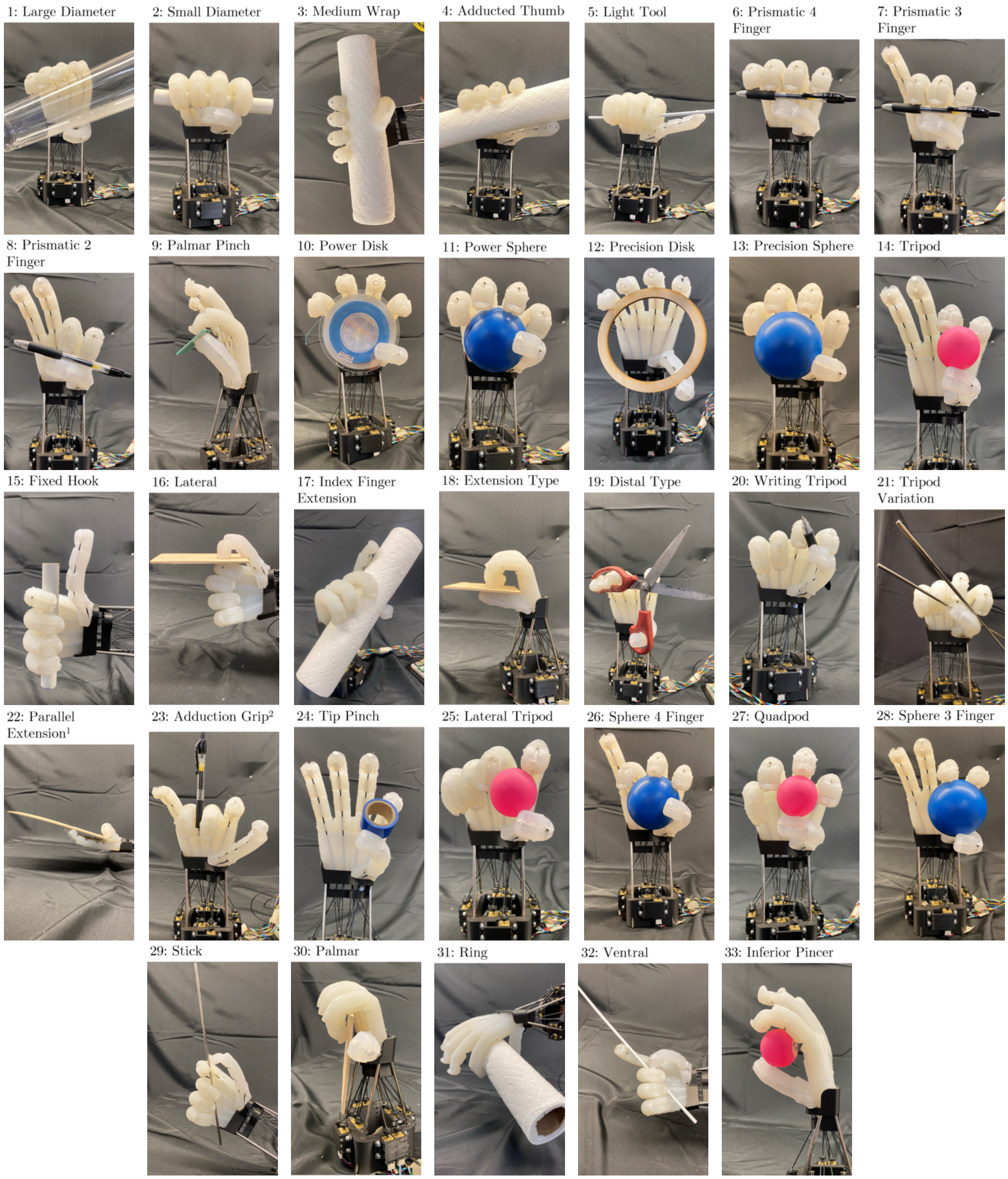

Figure 4.8: Achievable grasps from the Feix GRASP Taxonomy; grasps are numbered and labeled as described in [1]. [1] Failed grasp. Thumb was not capable of fully realized parallel extension. [2] Failed grasp. Adduction grip was maintained passively with the actuators not actively applying the force.

CHAPTER 5

CONCLUSION AND FUTURE WORK

5.1 Conclusion

5.1.1 Compliant, Large-Strain, and Self-Sensing TSAs

This thesis detailed the development of compliant, large-strain, and self-sensing TSAs and their application to soft robots. Firstly, these novel TSAs were designed, fabricated, and experimentally characterized. Secondly, models of the combined thermal- and twisting-based actuation were obtained under quasi-static inputs. Thirdly, models of the TSAs' self-sensing properties were obtained under quasi-static and transient (dynamic) inputs. These models accounted for the hysteresis, creep, and transient decay of the TSAs' electrical resistance. The models were verified to estimate the strain of the TSA with high accuracy.

5.1.2 TSA-Driven Soft Robots

Next, three TSA-driven soft robots were presented: a three-fingered gripper, a soft robotic manipulator, and an anthropomorphic soft gripper. This development of the soft manipulator entailed the design, fabrication, experimental characterization, modeling, and control. The performance of the manipulator was studied by experimentally analyzing the bending angle of the soft arm with respect to the number of twists (number of motor rotations) of the TSAs. The kinematic relationships between the TSA actuation and the manipulator's bending angle were modeled and experimentally verified. Similarly, the details for the three-fingered gripper and soft anthropomorphic gripper were briefly shown. The experimental results confirmed the high performance of the manipulator, which was largely due to the TSAs as the driving mechanism.

5.2 Future Work

5.2.1 Self-Sensing

Despite the high accuracy of the proposed self-sensing model, a more generalized model will be developed in future studies. Since the model in this study only considered a constant loading condition, future studies could account for arbitrary or even dynamic loads on the TSA. A preliminary experiment on the load-dependence of resistance showed that the load significantly affected the magnitudes of the hysteresis term of the resistance, but not the creep and transient decay. This was likely because increased loads (1) longitudinally stretched the TSA and (2) decreased the diameter of the TSA. In future work, each component of the model will be separately examined for its dependence on load. The findings of this study may potentially apply to other conductive materials that experience similar transient resistance decay [74, 93, 94]. Future work will also use the resistance as a feedback signal to control the length of the TSA.

Using resistance for strain estimation has two main advantages over motor encoders. If the TSA is constructed with stiff strings or only operates under a constant load, this strategy enables smaller DC motors without encoders to be utilized, which may result in reduced weight or mechanical complexity. More importantly, resistance sensing is advantageous when the TSA's strings are compliant or under varying loading conditions. A varying loading condition that stretches or shortens such TSA would be accompanied by a change in resistance, but not a change in motor angle. In future work, experiments will be conducted to predict both load and strain, given the resistance and twisting angle. This prediction may be realized by simultaneously solving two equations: the TSA dynamic model [31, 32] and strain–load–resistance model.

In the future, the proposed self-sensing model will be further improved to estimate the length of these TSAs also during thermal actuation. The potential coupling between resistance and temperature may present new challenges. In the meantime, the length of SCP-based TSAs actuated by only twisting can be accurately predicted via the resistance.

5.2.2 Thermal Actuation

Firstly, more operation methods of the proposed thermally-actuated TSAs may be studied in future work. In this study, the TSA was operated by first fully twisting and then applying power to the SCP strings to obtain additional strains. Other operational modes might prove to be more beneficial. For example, by twisting and heating the SCP strings at the same time, the TSA may contract more quickly, thus increasing its sufficient operational bandwidth.

Secondly, the repeatability and lifetime performance of the proposed TSAs may be formally tested in future work. Although existing studies have measured the maximum working cycles of the TSA with highly stiff strings [45], it is expected that the lifetime and repeatability may deteriorate with the usage of stretchable and coiled polymer strings.

5.2.3 TSA-Driven Soft Robots

Three-Fingered Compliant Gripper

Despite the capabilities of the robots in this study, further improvements can be made. For the three-fingered gripper, only twisting-induced actuation was used. In future studies, the combined thermally-induced and twisting-induced actuation could be implemented. In future work, thicker strings and stronger motors could be used which would allow the gripper to grasp heavier objects. In the work thus far, lightweight objects with masses of 100 g or less were gripped. Gripping objects that are heavy yet delicate could be a key advantage over traditional rigid grippers.

Soft Manipulator

For the soft robotic manipulator, several additional research avenues may be pursued.

- Multi-DOF closed-loop control could be developed to accurately control the pose of the manipulator in 3D space. In the current work, only single-DOF motion was controlled in a closed-loop. Furthermore, advanced control strategies could be examined, such as optimal control, adaptive control, or robust control.
- The development of a more advanced model with fewer assumptions and approximations could decrease the modeling error. For example, assumptions such as considering the relation between the axial force and motor angle to be linear

and assuming negligible effect from the inactive TSAs could be eliminated from the analysis to obtain a more accurate model.

- End-effectors could be developed for the soft manipulators, such a compliant gripper. With this end-effector, the pick-and-place capabilities of the gripper could be examined.

Anthropomorphic Gripper

Firstly, the design of the fingers and thumb could be modified to minimize the non-linear effects in their actuation profiles and to improve the grasping capabilities and the dexterity of the gripper. Additional controllable DOFs could also be included to improve the grasping performance and manipulation abilities of the gripper. Secondly, mathematical models could be developed to accurately predict the behavior of the gripper. Thirdly, the in-hand manipulation capabilities of the proposed robotic gripper could be further studied. For this purpose, advanced motion planning and grasping algorithms which utilize machine learning techniques [95, 96] could be developed. Finally, other soft robotic devices such as crawling robots or bipedal robots could be realized using TSAs.

BIBLIOGRAPHY

[1] T. Feix, J. Romero, H.-B. Schmiedmayer, A. M. Dollar, and D. Kragic, "The GRASP taxonomy of human grasp types," *IEEE Transactions on Human-Machine Systems*, vol. 46, no. 1, pp. 66–77, 2016.

[2] G. M. Whitesides, "Soft robotics," *Angewandte Chemie International Edition*, vol. 57, no. 16, pp. 4258–4273, 2018.

[3] J. Zhang, J. Sheng, C. O'Neill, C. J. Walsh, R. J. Wood, J. H. Ryu, J. P. Desai, and M. C. Yip, "Robotic artificial muscles: Current progress and future perspectives for biomimetic actuators," *IEEE Transactions on Robotics*, vol. 35, no. 3, pp. 761–781, 2019.

[4] B. Tondu, "What is an artificial muscle? A systemic approach.," *Actuators*, vol. 4, no. 4, pp. 336–352, 2015.

[5] S. M. Mirvakili and I. W. Hunter, "Artificial muscles: Mechanisms, applications, and challenges," *Advanced Materials*, vol. 30, no. 6, p. 1704407, 2018.

[6] J. Sun, B. Tighe, Y. Liu, and J. Zhao, "Twisted-and-coiled actuators with free strokes enable soft robots with programmable motions," *Soft Robotics*, vol. 8, no. 2, pp. 213–225, 2021.

[7] N. Kellaris, V. Gopaluni Venkata, G. M. Smith, S. K. Mitchell, and C. Keplinger, "Peano-HASEL actuators: Muscle-mimetic, electrohydraulic transducers that linearly contract on activation," *Science Robotics*, vol. 3, no. 14, 2018.

[8] P. Rothemund, N. Kellaris, S. K. Mitchell, E. Acome, and C. Keplinger, "HASEL artificial muscles for a new generation of lifelike robots—recent progress and future opportunities," *Advanced Materials*, vol. 33, no. 19, 2021.

[9] Z. Ye, Z. Chen, R. Asmatulu, and H. Chan, "Robust control of dielectric elastomer diaphragm actuator for human pulse signal tracking," *Smart Materials and Structures*, vol. 26, no. 8, p. 085043, 2017.

[10] H. Rodrigue, W. Wang, M. W. Han, T. J. Y. Kim, and S. H. Ahn, "An overview of shape memory alloy-coupled actuators and robots," *Soft Robotics*, vol. 4, no. 1, pp. 3–15, 2017.

[11] M. C. Yip and G. Niemeyer, "On the control and properties of supercoiled polymer artificial muscles," *IEEE Transactions on Robotics*, vol. 33, no. 3, pp. 689–699, 2017.

[12] X. Tang, K. Li, Y. Liu, D. Zhou, and J. Zhao, "A general soft robot module driven by twisted and coiled actuators," *Smart Materials and Structures*, vol. 28, no. 3, p. 035019, 2019.

[13] W. S. Chu, K. T. Lee, S. H. Song, M. W. Han, J. Y. Lee, H. S. Kim, M. S. Kim, Y. J. Park, K. J. Cho, and S. H. Ahn, "Review of biomimetic underwater robots using smart actuators," *Int. J. Precis. Eng. Manuf.*, vol. 13, no. 7, pp. 1281–1292, 2012.

[14] J.-H. Koo, A. Dawson, and H.-J. Jung, "Characterization of actuation properties of magnetorheological elastomers with embedded hard magnetic particles," *Journal of Intelligent Material Systems and Structures*, vol. 23, no. 9, pp. 1049–1054, 2012.

[15] T. Kikuchi, K. Otsuki, J. Furusho, H. Abe, J. Noma, M. Naito, and N. Lauzier, "Development of a compact magnetorheological fluid clutch for human-friendly actuator," *Adv. Robot.*, vol. 24, no. 10, pp. 1489–1502, 2010.

[16] B. Shih, D. Drotman, C. Christianson, Z. Huo, R. White, H. I. Christensen, and M. T. Tolley, "Custom soft robotic gripper sensor skins for haptic object visualization," in *2017 IEEE/RSJ International Conference on Intelligent Robots and Systems (IROS)*, pp. 494–501, 2017.

[17] Y. Tang, Y. Chi, J. Sun, T.-H. Huang, O. H. Maghsoudi, A. Spence, J. Zhao, H. Su, and J. Yin, "Leveraging elastic instabilities for amplified performance: Spine-inspired high-speed and high-force soft robots," *Science Advances*, vol. 6, no. 19, 2020.

[18] Y. She, C. Li, J. Cleary, and H.-J. Su, "Design and fabrication of a soft robotic hand with embedded actuators and sensors," *Journal of Mechanisms and Robotics*, vol. 7, no. 2, 2015.

[19] C. Laschi, M. Cianchetti, B. Mazzolai, L. Margheri, M. Follador, and P. Dario, "Soft robot arm inspired by the octopus," *Advanced Robotics*, vol. 27, no. 7, pp. 709–727, 2012.

[20] C. Majidi, "Soft robotics: a perspective—current trends and prospects for the future," *Soft Robotics*, vol. 1, no. 1, pp. 5–11, 2014.

[21] Y. Almubarak and Y. Tadesse, "Twisted and coiled polymer (TCP) muscles embedded in silicone elastomer for use in soft robot," *International Journal of Intelligent Robotics and Applications*, vol. 1, no. 3, pp. 352–368, 2017.

[22] B. Pawlowski, J. Sun, J. Xu, Y. Liu, and J. Zhao, "Modeling of soft robots actuated by twisted-and-coiled actuators," *IEEE/ASME Transactions on Mechatronics*, vol. 24, no. 1, pp. 5–15, 2019.

[23] S. Chen, Y. Cao, M. Sarparast, H. Yuan, L. Dong, X. Tan, and C. Cao, "Soft crawling robots: Design, actuation, and locomotion," *Advanced Materials Technologies*, vol. 5, no. 2, p. 1900837, 2020.

[24] D. S. Shah, J. P. Powers, L. G. Tilton, S. Kriegman, J. Bongard, and R. Kramer-Bottiglio, "A soft robot that adapts to environments through shape change," *Nature Machine Intelligence*, vol. 3, no. 1, pp. 51–59, 2021.

[25] R. F. Shepherd, F. Ilievski, W. Choi, S. A. Morin, A. A. Stokes, A. D. Mazzeo, X. Chen, M. Wang, and G. M. Whitesides, "Multigait soft robot," *Proceedings of the National Academy of Sciences*, vol. 108, no. 51, pp. 20400–20403, 2011.

[26] Y. Hao, S. Biswas, E. W. Hawkes, T. Wang, M. Zhu, L. Wen, and Y. Visell, "A multimodal, enveloping soft gripper: Shape conformation, bioinspired adhesion, and expansion-driven suction," *IEEE Transactions on Robotics*, vol. 37, no. 2, pp. 350–362, 2020.

[27] Y. Cui, X.-J. Liu, X. Dong, J. Zhou, and H. Zhao, "Enhancing the universality of a pneumatic gripper via continuously adjustable initial grasp postures," *IEEE Transactions on Robotics*, pp. 1–15, ahead of print, http://doi.org/10.1109/TRO.2021.3060969.

[28] D. Rus and M. T. Tolley, "Design, fabrication and control of soft robots," *Nature*, vol. 521, no. 7553, pp. 467–475, 2015.

[29] S. Abondance, C. B. Teeple, and R. J. Wood, "A dexterous soft robotic hand for delicate in-hand manipulation," *IEEE Robotics and Automation Letters*, vol. 5, no. 4, pp. 5502–5509, 2020.

[30] M. A. Graule, T. P. McCarthy, C. B. Teeple, J. Werfel, and R. J. Wood, "Somogym: A toolkit for developing and evaluating controllers and reinforcement learning algorithms for soft robots," *IEEE Robotics and Automation Letters*, vol. 7, no. 2, pp. 4071–4078, 2022.

[31] G. Palli, C. Natale, C. May, C. Melchiorri, and T. Wurtz, "Modeling and control of the twisted string actuation system," *IEEE/ASME Transactions on Mechatronics*, vol. 18, no. 2, pp. 664–673, 2013.

[32] I. Gaponov, D. Popov, and J. H. Ryu, "Twisted string actuation systems: A study of the mathematical model and a comparison of twisted strings," *IEEE/ASME Transactions on Mechatronics*, vol. 19, no. 4, pp. 1331–1342, 2014.

[33] T. Tsabedze, E. Hartman, and J. Zhang, "A compact, compliant, and biomimetic robotic assistive glove driven by twisted string actuators," *International Journal of Intelligent Robotics and Applications*, vol. 5, no. 3, pp. 381–394, 2021.

[34] A. Pepe, M. Hosseini, U. Scarcia, G. Palli, and C. Melchiorri, "Development of a haptic interface based on twisted string actuators," in *2017 IEEE International Conference on Advanced Intelligent Mechatronics (AIM)*, pp. 28–33, IEEE, 2017.

[35] G. Palli, C. Melchiorri, G. Vassura, U. Scarcia, L. Moriello, G. Berselli, A. Cavallo, G. De Maria, C. Natale, S. Pirozzi, *et al.*, "The DEXMART hand: Mechatronic design and experimental evaluation of synergy-based control for human-like grasping," *The International Journal of Robotics Research*, vol. 33, no. 5, pp. 799–824, 2014.

[36] H.-S. Seong, D.-H. Kim, I. Gaponov, and J.-H. Ryu, "Development of a twisted string actuator-based exoskeleton for hip joint assistance in lifting tasks," in *2020 IEEE International Conference on Robotics and Automation (ICRA)*, pp. 761–767, IEEE, 2020.

[37] S. Nedelchev, I. Gaponov, and J.-H. Ryu, "Accurate dynamic modeling of twisted string actuators accounting for string compliance and friction," *IEEE Robotics and Automation Letters*, vol. 5, no. 2, pp. 3438–3443, 2020.

[38] T. Inoue, S. Yamamoto, R. Miyata, and S. Hirai, "Robotic joint design by agonist and antagonist arrangement with twisting small-diameter round-belts," in *2015 IEEE/RSJ International Conference on Intelligent Robots and Systems (IROS)*, pp. 1751–1756, 2015.

[39] C. Laschi, B. Mazzolai, and M. Cianchetti, "Soft robotics: Technologies and systems pushing the boundaries of robot abilities," *Science Robotics*, vol. 1, no. 1, 2016.

[40] J. Luong, P. Glick, A. Ong, M. S. deVries, S. Sandin, E. W. Hawkes, and M. T. Tolley, "Eversion and retraction of a soft robot towards the exploration of coral reefs," in *Proc. IEEE Int. Conf. Soft Robot.*, pp. 801–807, 2019.

[41] Y. M. Zhou, D. Wagner, K. Nuckols, R. Heimgartner, C. Correia, M. Clarke, D. Orzel, C. O'Neill, R. Solinsky, S. Paganoni, and C. J. Walsh, "Soft robotic

glove with integrated sensing for intuitive grasping assistance post spinal cord injury," in *Proc. IEEE Int. Conf. Robot. Autom.*, pp. 9059–9065, 2019.

[42] M. Kim, C. Liu, J. Kim, S. Lee, A. Meguid, C. J. Walsh, and S. Kuindersma, "Bayesian optimization of soft exosuits using a metabolic estimator stopping process," in *Proc. IEEE Int. Conf. Robot. Autom.*, pp. 9173–9179, 2019.

[43] E. T. Roche, M. A. Horvath, I. Wamala, A. Alazmani, S.-E. Song, W. Whyte, Z. Machaidze, C. J. Payne, J. C. Weaver, G. Fishbein, J. Kuebler, N. V. Vasilyev, D. J. Mooney, F. A. Pigula, and C. J. Walsh, "Soft robotic sleeve supports heart function," *Sci. Transl. Med.*, vol. 9, no. 373, 2017.

[44] S. H. Jeong, K. S. Kim, and S. Kim, "Designing anthropomorphic robot hand with active dual-mode twisted string actuation mechanism and tiny tension sensors," *IEEE Robot. Autom. Lett.*, vol. 2, no. 3, pp. 1571–1578, 2017.

[45] M. Usman, H. Seong, B. Suthar, I. Gaponov, and J.-H. Ryu, "A study on life cycle of twisted string actuators: Preliminary results," in *2017 IEEE/RSJ International Conference on Intelligent Robots and Systems (IROS)*, pp. 4680–4685, 2017.

[46] D. Bombara, V. Mansurov, R. Konda, S. Fowzer, and J. Zhang, "Self-sensing for twisted string actuators using conductive supercoiled polymers," in *Proceedings of the ASME Conference Smart Materials, Adaptive Structures and Intelligent Systems*, Paper SMASIS2019-5587, 2019.

[47] I. Godler and T. Sonoda, "A five fingered robotic hand prototype by using twist drive," in *ISR 2010 (41st International Symposium on Robotics) and ROBOTIK 2010 (6th German Conference on Robotics)*, pp. 1–6, 2010.

[48] T. Wurtz, C. May, B. Holz, C. Natale, G. Palli, and C. Melchiorri, "The twisted string actuation system: Modeling and control," in *Proceedings of IEEE/ASME International Conference on Advanced Intelligent Mechatronics*, pp. 1215–1220, 2010.

[49] D. Popov, I. Gaponov, and J. Ryu, "Bidirectional elbow exoskeleton based on twisted-string actuators," in *2013 IEEE/RSJ International Conference on Intelligent Robots and Systems*, pp. 5853–5858, 2013.

[50] M. Hosseini, R. Meattini, A. San-Millan, G. Palli, C. Melchiorri, and J. Paik, "A sEMG-driven soft exosuit based on twisted string actuators for elbow assistive

applications," *IEEE Robotics and Automation Letters*, vol. 5, no. 3, pp. 4094–4101, 2020.

[51] C. S. Haines, M. D. Lima, N. Li, G. M. Spinks, J. Foroughi, J. D. Madden, S. H. Kim, S. Fang, M. Jung de Andrade, F. Göktepe, *et al.*, "Artificial muscles from fishing line and sewing thread," *Science*, vol. 343, no. 6173, pp. 868–872, 2014.

[52] M. Hiraoka, K. Nakamura, H. Arase, K. Asai, Y. Kaneko, S. W. John, K. Tagashira, and A. Omote, "Power-efficient low-temperature woven coiled fibre actuator for wearable applications," *Scientific reports*, vol. 6, no. 1, pp. 1–9, 2016.

[53] Y. Yang, Z. Kan, Y. Zhang, *et al.*, "A novel variable stiffness actuator based on pneumatic actuation and supercoiled polymer artificial muscles," in *Proceedings of IEEE International Conference on Robotics and Automation*, pp. 3983–3989, 2019.

[54] K. H. Cho, Y. Kim, S. Y. Yang, *et al.*, "Artificial musculoskeletal actuation module driven by twisted and coiled soft actuators," *Smart Materials and Structures*, vol. 28, no. 12, p. 125010, 2019.

[55] J. Zhang, K. Iyer, A. Simeonov, and M. C. Yip, "Modeling and inverse compensation of hysteresis in super-coiled polymer artificial muscles," *IEEE Robotics and Automation Letters*, vol. 2, no. 2, pp. 773–780, 2017.

[56] A. Simeonov, T. Henderson, Z. Lan, *et al.*, "Bundled super-coiled polymer artificial muscles: Design, characterization, and modeling," *IEEE Robot. Autom. Lett.*, vol. 3, no. 3, pp. 1671–1678, 2018.

[57] J. Zhao and A. Abbas, "A low-cost soft coiled sensor for soft robots," in *Proceedings of ASME Dynamic Systems and Control Conference*, Paper DSCC2016-9916, 2016.

[58] A. Abbas and J. Zhao, "Twisted and coiled sensor for shape estimation of soft robots," in *Proc. IEEE/RSJ Int. Conf. Intell. Robot. Syst.*, pp. 482–487, Sep. 2017.

[59] X. Tang, K. Li, Y. Liu, and J. Zhao, "Coiled conductive polymer fiber used in soft manipulator as sensor," *IEEE Sensors Journal*, vol. 18, pp. 6123–6129, Aug 2018.

[60] W. Crooks, G. Vukasin, M. O'Sullivan, W. Messner, and C. Rogers, "Fin Ray®

effect inspired soft robotic gripper: From the Robosoft Grand Challenge toward optimization," *Frontiers in Robotics and AI*, vol. 3, p. 70, 2016.

[61] G. Palli, M. Hosseini, L. Moriello, and C. Melchiorri, "Modeling and identification of a variable stiffness joint based on twisted string actuators," in *2015 IEEE/RSJ International Conference on Intelligent Robots and Systems (IROS)*, pp. 1757–1762, IEEE, 2015.

[62] J. Zhang, D. Bombara, S. Fowzer, and C. Brennan, "Compliant and large-strain twisted string actuators using supercoiled polymers," in *2020 3rd IEEE International Conference on Soft Robotics (RoboSoft)*, pp. 201–207, IEEE, 2020.

[63] D. Bombara, S. Fowzer, and J. Zhang, "Compliant, large-strain, and self-sensing twisted string actuators," *Soft Robotics*, vol. 9, no. 1, pp. 72–88, 2022.

[64] D. Bombara, R. Konda, and J. Zhang, "Experimental characterization and modeling of the self-sensing property in compliant twisted string actuators," *IEEE Robotics and Automation Letters*, vol. 6, no. 2, pp. 974–981, 2021.

[65] D. Popov, I. Gaponov, and J. H. Ryu, "Towards variable stiffness control of antagonistic twisted string actuators," in *Proceedings of IEEE/RSJ International Conference on Intelligent Robots and Systems*, pp. 2789–2794, 2014.

[66] R. Konda and J. Zhang, "The effects of nylon polymer threads on hysteresis behavior of supercoiled polymer (SCP) artificial muscles," in *Proceedings of the ASME Dynamic Systems and Control Conference*, Paper DSCC2019-9169, 2019.

[67] T. A. Luong, K. H. Cho, M. G. Song, J. C. Koo, H. R. Choi, and H. Moon, "Nonlinear Tracking Control of a Conductive Supercoiled Polymer Actuator," *Soft Robotics*, vol. 5, pp. 190–203, Nov. 2017.

[68] D. G. Hunt and M. W. Darlington, "Prediction of creep of nylon-6,6 at constant stress, temperature and moisture content," *Polymer*, vol. 20, no. 2, pp. 241 – 246, 1979.

[69] A. Abbas and J. Zhao, "A physics based model for twisted and coiled actuator," in *Proceeding of the IEEE International Conference on Robotics and Automation*, pp. 6121–6126, 2017.

[70] A. Charles and S. Matthew, *Fundamentals of Electric Circuits*, p. 212. McGraw-Hill, 2004.

[71] R. Kohlrausch, "Theorie des elektrischen rückstandes in der leidener flasche," *Annalen der Physik*, vol. 167, no. 2, pp. 179–214, 1854.

[72] I. Mayergoyz, *Mathematical Models of Hysteresis*. Springer-Verlag, 1991.

[73] X. Tan and J. Baras, "Modeling and control of hysteresis in magnetostrictive actuators," *Automatica*, vol. 40, no. 9, pp. 1469–1480, 2004.

[74] G. Heo, K.-h. Pyo, D. H. Lee, Y. Kim, and J.-W. Kim, "Critical Role of Diels–Adler Adducts to Realise Stretchable Transparent Electrodes Based on Silver Nanowires and Silicone Elastomer," *Scientific Reports*, vol. 6, p. 25358, May 2016.

[75] M. Al Janaideh, S. Rakheja, and C. Su, "An analytical generalized Prandtl–Ishlinskii model inversion for hysteresis compensation in micropositioning control," *IEEE/ASME Transactions on Mechatronics*, vol. 16, pp. 734–744, Aug 2011.

[76] B. Mokaberi and A. A. G. Requicha, "Compensation of scanner creep and hysteresis for AFM nanomanipulation," *IEEE Transactions on Automation Science and Engineering*, vol. 5, no. 2, pp. 197–206, 2008.

[77] J. Zhang, A. Simeonov, and M. C. Yip, "Three-dimensional hysteresis compensation enhances accuracy of robotic artificial muscles," *Smart Materials and Structures*, vol. 27, p. 035002, jan 2018.

[78] J. Zhang, D. Torres, J. L. Ebel, *et al.*, "A composite hysteresis model in self-sensing feedback control of fully integrated VO_2 microactuators," *IEEE/ASME Transactions on Mechatronics*, vol. 21, no. 5, pp. 2405–2417, 2016.

[79] Y. Shan and K. K. Leang, "Accounting for hysteresis in repetitive control design: Nanopositioning example," *Automatica*, vol. 48, no. 8, pp. 1751 – 1758, 2012.

[80] R. Iyer and X. Tan, "Control of hysteretic systems through inverse compensation," *IEEE Contr. Syst. Mag.*, vol. 29, no. 1, pp. 83–99, 2009.

[81] C. Wu and W. Zheng, "A modeling of twisted and coiled polymer artificial muscles based on elastic rod theory," *Actuators*, vol. 9, p. 25, Apr. 2020.

[82] A. Cherubini, G. Moretti, R. Vertechy, and M. Fontana, "Experimental characterization of thermally-activated artificial muscles based on coiled nylon fishing lines," *AIP Advances*, vol. 5, p. 067158, June 2015.

[83] M. A. Janaideh, C.-Y. Su, and S. Rakheja, "Development of the rate-dependent Prandtl–Ishlinskii model for smart actuators," *Smart Materials and Structures*, vol. 17, p. 035026, Apr 2008.

[84] M. Rakotondrabe, C. Clevy, and P. Lutz, "Complete open loop control of hysteretic, creeped, and oscillating piezoelectric cantilevers," *IEEE Transactions on Automation Science and Engineering*, vol. 7, no. 3, pp. 440–450, 2010.

[85] R. Waltz, J. Morales, J. Nocedal, and D. Orban, "An interior algorithm for nonlinear optimization that combines line search and trust region steps," *Mathematical Programming*, vol. 107, pp. 391–408, July 2006.

[86] D. Bombara, R. Konda, E. Chow, and J. Zhang, "Physics-based kinematic modeling of a twisted string actuator-driven soft robotic manipulator," *2022 American Control Conference*, 2022. under review.

[87] M. W. Hannan and I. D. Walker, "Kinematics and the implementation of an elephant's trunk manipulator and other continuum style robots," *Journal of Robotic Systems*, vol. 20, no. 2, pp. 45–63, 2003.

[88] A. San-Millan Rodriguez, M. Hosseini, and J. Paik, "A hybrid control strategy for force and precise end effector positioning of a twisted string actuator," *IEEE/ASME Transactions on Mechatronics*, early access, Dec. 24, 2020.

[89] U. Mehmood, D. Popov, I. Gaponov, and J. H. Ryu, "Rotational twisted string actuator with linearized output: Mathematical model and experimental evaluation," *IEEE/ASME International Conference on Advanced Intelligent Mechatronics, AIM*, pp. 1072–1077, 2015.

[90] A. Savitzky and M. J. E. Golay, "Smoothing and differentiation of data by simplified least squares procedures.," *Analytical Chemistry*, vol. 36, no. 8, pp. 1627–1639, 1964.

[91] H. Zhou, A. Mohammadi, D. Oetomo, and G. Alici, "A novel monolithic soft robotic thumb for an anthropomorphic prosthetic hand," *IEEE Robotics and Automation Letters*, vol. 4, no. 2, pp. 602–609, 2019.

[92] R. Deimel and O. Brock, "A novel type of compliant and underactuated robotic hand for dexterous grasping," *The International Journal of Robotics Research*, vol. 35, no. 1-3, pp. 161–185, 2016.

[93] T. N. Tallman, S. Gungor, K. W. Wang, and C. E. Bakis, "Tactile imaging

and distributed strain sensing in highly flexible carbon nanofiber/polyurethane nanocomposites," *Carbon*, vol. 95, pp. 485–493, 2015.

[94] R. Zhang, H. Deng, R. Valenca, J. Jin, Q. Fu, E. Bilotti, and T. Peijs, "Strain sensing behavior of elastomeric composite films containing carbon nanotubes under cyclic loading," *Composite Science and Technology*, vol. 74, pp. 1–5, 2013.

[95] K. Chin, T. Hellebrekers, and C. Majidi, "Machine learning for soft robotic sensing and control," *Advanced Intelligent Systems*, vol. 2, no. 6, p. 1900171, 2020.

[96] D. Kim, S.-H. Kim, T. Kim, B. B. Kang, M. Lee, W. Park, S. Ku, D. Kim, J. Kwon, H. Lee, J. Bae, Y.-L. Park, K.-J. Cho, and S. Jo, "Review of machine learning methods in soft robotics," *PLOS ONE*, vol. 16, pp. 1–24, 02 2021.